Sussex Research Online

Techniques used to search for a permanent electric dipole moment of the 199 Hg atom and the implications for CP violation

Article (Unspecified)

Techniques used to search for a permanent electric dipole moment of the ^{199}Hg atom and the implications for *CP* violation

M. D. Swallows,[*] T. H. Loftus,[*] W. C. Griffith,[†] B. R. Heckel, and E. N. Fortson

Department of Physics, Box 351560, University of Washington, Seattle, Washington 98195-1560, USA

M. V. Romalis

Department of Physics, Princeton Univeristy, Princeton, New Jersey 02138-1234, USA

We discuss in detail the search for a permanent electric dipole moment (EDM) of the ^{199}Hg atom reported by Griffith *et al.* [Phys. Rev. Lett. **102**, 101601 (2009)]. The upper bound, $d(^{199}\text{Hg}) < 3.1 \times 10^{-29}$ *e* cm (95% C.L.), is a factor of 7 improvement over the best previous EDM limit for ^{199}Hg, provides the most sensitive probe to date for EDMs in diamagnetic atoms, and sets new limits on time-reversal symmetry violation in extensions to the standard model. This paper provides extensive discussion of the techniques used to search for the ^{199}Hg EDM and the implications of the new ^{199}Hg EDM limit for *CP* violation in elementary particle interactions.

I. INTRODUCTION

A permanent electric dipole moment (EDM) of an elementary particle or atom would violate time reversal (*T*) symmetry and would also signal a violation of the combined symmetries of charge conjugation and parity (*CP*) through the *CPT* theorem. *CP* violation has been incorporated into the standard model (SM) by means of a complex phase in the Cabibo-Kobayashi-Maskawa (CKM) quark-mixing matrix [1]. The CKM phase accounts phenomenologically for the *CP* violation observed in flavor-changing processes such as the decay of *K* and *B* mesons [2,3], but this mechanism affects flavor-conserving processes only at higher order, and thus predicts EDMs that are vanishingly small compared with current experimental limits.

A more severe breaking of *CP* symmetry, however, is needed to account for baryogenesis, or the observed matter-antimatter asymmetry of the universe [4], and many theories beyond the SM naturally allow for additional *CP* violation that could generate EDMs large enough to measure with current technology. For this reason, EDM searches are well positioned to provide background-free probes for physics beyond the SM.

EDM searches are under way in a variety of systems, most notably bare neutrons, diamagnetic atoms, paramagnetic atoms and molecules, and solid-state spin systems [5,6]. The different systems provide different sensitivities to underlying sources of *CP* violation and together place stringent limits on *CP* violation beyond the SM.

In a recent article [7] we reported the results from a new search for the EDM of the ^{199}Hg atom: $d(^{199}\text{Hg}) < 3.1 \times 10^{-29}$ *e* cm (95% C.L.), corresponding to a sevenfold improvement on the best previous limit [8]. This experiment provides the most sensitive probe to date for EDMs in diamagnetic atoms and sets new limits on time-reversal symmetry violation in extensions to the SM. In the present

work, we significantly expand upon the Ref. [7] discussion and provide comprehensive descriptions of the ^{199}Hg EDM search apparatus, the techniques used to collect and analyze the EDM search data, possible sources for systematic errors, and finally, the implications of the new ^{199}Hg EDM limit for extensions to the SM.

The remainder of this paper is organized as follows. Section II introduces the basic principles of the experiment. Section III gives an overview of the experimental apparatus and EDM search technique and provides details regarding the magnetic shielding, bias magnetic field generation and control, high voltage (HV) supply, ^{199}Hg vapor cells, the vapor cell containment vessels, and leakage current measurement systems. Section IV describes the data acquisition and analysis techniques while Sec. V outlines the system sensitivity and noise floor. The ^{199}Hg EDM data set is discussed in Sec. VI, while systematic effects form the focus of Sec. VII. The current limit on the ^{199}Hg EDM is given in Sec. VIII. Finally, Sec. IX outlines the implications of the measurement for *CP* violation in extensions to the SM. Some concluding remarks and thoughts on future prospects are given in Sec. X. A short appendix discusses testing of materials for ferromagnetic impurities.

II. BASIC PRINCIPLES OF THE EXPERIMENT

^{199}Hg has a $^1S_0$ electronic ground state and nuclear spin-$\frac{1}{2}$. An EDM of the ground state must point along the nuclear spin axis. The Larmor frequency for spin-polarized ^{199}Hg atoms immersed in parallel or antiparallel magnetic and electric fields is given by

$$h\nu_L = 2|\mu B \pm dE|, \tag{1}$$

where h is Planck's constant, B and E are the magnetic and electric field amplitudes, μ and d are the ^{199}Hg magnetic and electric dipole moments, and $+(-)$ denotes parallel (antiparallel) fields. The signature for $d \neq 0$ is an electric-field correlated change to the Larmor frequency when $\boldsymbol{E}$ is reversed relative to $\boldsymbol{B}$. Systems such as ^{199}Hg with spin-$\frac{1}{2}$ are particularly attractive since the only possible moments in the

---

[*]Present address: AOSense, Inc., Sunnyvale, California 94085, USA.

[†]Present address: Subatomic Physics Group, Los Alamos National Laboratory, Los Alamos, New Mexico 87545, USA.
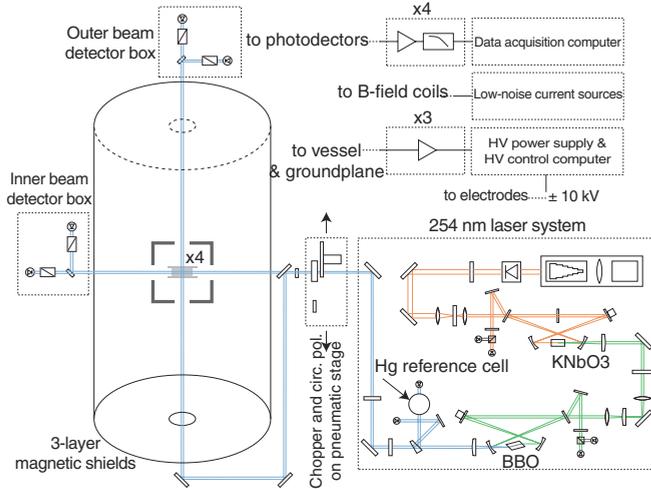
FIG. 1. (Color online) Pictorial diagram of the EDM search apparatus. The boxed areas represent the frequency-quadrupled UV laser system, the three-layer high-permeability magnetic shields, the HV power supply, the low-noise current sources, and the vapor-cell containment vessel.

ground state are the magnetic and electric dipole moments listed in Eq. (1); for systems with spin $> \frac{1}{2}$, higher-order moments allow additional interactions that, in turn, broaden the range of possible systematic effects.

A fundamental limitation to the sensitivity of the experiment is set by atomic shot noise. As shown in Sec. V A, the ideal shot-noise uncertainty is

$$\delta d = \frac{\hbar}{2E\sqrt{2NTt}}, \tag{2}$$

where N is the number of independent atomic systems participating in the measurement, T is the coherence time (here taken to be the time used for a single measurement of the Larmor frequency), and t is the total integration time. According to Eq. (2), the sensitivity is improved by performing the measurement with a large number of atoms, maximizing the coherence time T, and repeating the measurement a large number of times ($\simeq t/T$). The statistical sensitivity is optimized by maximizing the spin coherence time, number of particles, and electric field strength.

The statistical uncertainty in the result of the ^{199}Hg search discussed here (see Sec. VI) is 1.29×10^{-29} e cm, corresponding to an absolute energy shift of roughly 0.1 nHz, among the smallest ever measured. However, this uncertainty is still a factor of 25 larger than the fundamental sensitivity limit given by Eq. (2) for this measurement, which is $\sim 3 \times 10^{-31}$ e cm for the integration time used, corresponding to a shift of ~ 3 pHz.

III. EXPERIMENTAL APPARATUS AND TECHNIQUES

Our apparatus (see Fig. 1) uses a stack of four spin-polarized Hg vapor cells to search for the EDM-induced frequency shift predicted by Eq. (1). All four cells lie in a uniform bias magnetic field. The region containing the cells is isolated from external B-field fluctuations by several layers of high-permeability magnetic shielding. Oppositely directed electric

fields are applied to the two middle cells, resulting in an EDM-sensitive frequency difference between the cells,

$$\delta \nu = \frac{4dE}{h}. \tag{3}$$

The Larmor frequencies in the two cells are measured simultaneously, and $h/(4E) = 1.14 \times 10^{-19}$ e cm/Hz for the middle cell electrode spacing of 1.1 cm and typically employed potential difference of ± 10 kV. The two outer cells, enclosed by the HV electrodes and thus placed at $E = 0$, are insensitive to EDM effects and instead act as comagnetometers that allow the cancellation of noise due to B-field gradients and checks for spurious HV-correlated B-field shifts.

Single experimental cycles (termed scans) are divided into pump and probe phases. During the pump phase, a 254-nm laser is tuned to the $6\,^1S_0 \rightarrow 6\,^3P_1(F = 1/2)$ transition in ^{199}Hg and, in each cell, modulated-intensity transverse pumping [9,10] is used to build up spin polarization in a frame rotating about the magnetic field. During this phase, roughly 30 μW of circularly polarized light, modulated by a chopper wheel with a $\sim 30\%$ duty cycle, is incident on each cell. After 30 s of optical pumping, the laser is switched to a probe configuration: The polarization is switched from circular to linear, the detuning is increased to $+10$ GHz, and the per-cell power is lowered to ~ 3 μW. During the probe phase, the spin polarization precesses about the magnetic field and induces, via optical rotation synchronous with the Larmor frequency, rotation of the plane of polarization for the linearly polarized probe beams. These rotations are converted to amplitude-modulated signals (from which the Larmor frequencies are extracted) with UV-sensitive photodiodes placed after linear polarizers. This basic pump-probe process is repeated several hundred times over the course of an individual experimental run.

In the following sections, we detail the techniques used to spin polarize and observe Larmor precession of the ^{199}Hg atoms and the various apparatus subsystems including the 254-nm laser, the Hg vapor cells and vapor-cell enclosure, the magnetic shielding and bias magnetic field coils and controls, the HV delivery system, and the leakage current monitors.

A. Transverse optical pumping

In standard optical pumping experiments, ground-state Zeeman polarization is established with circularly polarized light directed along the magnetic field, that is, with $\hat{k} \cdot \hat{b} = 1$, where $\hat{k}$ and $\hat{b}$ are the light-beam k-vector and B-field unit vector, respectively. Observing Larmor precession about the magnetic field (as described in the next section) then requires rotating $\hat{b}$ such that $\hat{k} \cdot \hat{b} = 0$. Changing $\hat{b}$, however, inevitably degrades the magnetic field stability and hence leads to increased Larmor frequency noise. Transverse optical pumping [9] solves this problem: Circularly polarized resonance light with $\hat{k} \cdot \hat{b} = 0$ is amplitude modulated at the Larmor frequency, which establishes spin polarization rotating at the Larmor frequency in a plane perpendicular to $\hat{b}$.

Any fluorescence from atoms excited by the pumping light could be reabsorbed and reduce the spin polarization. In the vapor cells used here, however, collisions with a carbon

monoxide (CO) buffer gas efficiently quench the excited-state atoms to the ground state before they can emit fluorescence.

The spin-$\frac{1}{2}$ Hg nuclei can be modeled as an ensemble of classical magnetic moments with a Bloch equation given by

$$\frac{d\boldsymbol{P_a}}{dt} = \Gamma_p(\boldsymbol{P_l} - \boldsymbol{P_a}) - \Gamma_r \boldsymbol{P_a} - \gamma \boldsymbol{P_a} \times \boldsymbol{B}, \qquad (4)$$

where $\boldsymbol{P_a}$ is the atomic polarization vector, $\boldsymbol{P_l}$ is a vector describing the light circular polarization, and γ is the gyromagnetic ratio in units of angular frequency per magnetic field. The light polarization vector $\boldsymbol{P_l} = P_l \hat{k}$ is oriented along the light propagation direction, and has a magnitude equal to the fractional circular polarization of the light, $P_l = (n_{\sigma+} - n_{\sigma-})/(n_{\sigma+} + n_{\sigma-})$, where $n_{\sigma\pm}$ is the number of $\sigma_\pm$-polarized photons in the beam. On/off modulation of the pumping light is modeled by multiplying the pumping rate Γ_p by a unit step function:

$$U[\cos(2\pi\nu_m t) - \cos(\delta\theta/2)], \quad U(x) = \begin{cases} 0, & x < 0, \\ 1, & x > 0, \end{cases} \quad (5)$$

where ν_m is the modulation frequency and $\delta\theta$ specifies the modulation duty cycle: $\delta\theta = \pi$ corresponds to a duty cycle of 50%. For $\nu_m = \nu_L$ and in the steady-state limit, the fractional polarization attains a maximum value P_F given by

$$P_F \sim \frac{f_1\Gamma_p}{f_1\Gamma_p + f_2\Gamma_p + \Gamma_r}, \qquad (6)$$

where $f_1 = (\delta\theta/2)\sin(\delta\theta/2)$ and $f_2 = (\delta\theta/2)[1 - \cos(\delta\theta/2)]$ account for the reduced pumping efficiency and light-induced depolarization that occur when, as $\boldsymbol{P_a}$ rotates, $\hat{k} \cdot (\boldsymbol{P_a}/P_a) \neq 1$. Γ_r gives the rate at which relaxation processes (such as cell wall collisions or spin diffusion due to magnetic field gradients) destroy $\boldsymbol{P_a}$. During and after the pumping process, the spins precess in a plane normal to the B field at the angular Larmor frequency $\omega_L = \gamma B$; after extinction of the pump light, the spin magnitude decays as $P_a(t) = P_a(0)e^{-\Gamma t}$, where $\Gamma > \Gamma_r$ is the total spin relaxation rate during the probe phase and includes the effect of spin-depolarization due to probe light absorption.

Figure 2 shows the ^{199}Hg fractional ground-state nuclear polarization versus time for several values of the duty cycle $\delta\theta$. The curves were obtained by numerically integrating Eq. (4) with $\nu_m = \nu_L$ and per-atom pumping and relaxation rates typical for the experiment, namely, $\Gamma_p = 0.5$ s^{-1} and $\Gamma_r = 1/200$ s^{-1}. In general, the polarization evolves as

$$P_A(t) = P_F\left[1 - \exp\left(-\frac{\Gamma_p\delta\theta}{2\pi}t\right)\right], \qquad (7)$$

where the factor of $\delta\theta/(2\pi)$ accounts for the reduction to Γ_p resulting from the fractional on/off time for the pumping light. As implied by this expression and shown in the plot, increasing $\delta\theta$ decreases the time required to reach steady state, but reduces the equilibrium polarization. Conversely, decreasing $\delta\theta$ increases the final polarization, but at the cost of increased pump-up time: The light is only on when the atoms are nearly parallel to the light propagation direction $\hat{k}$. These competing processes lead, for the experimentally utilized pump time of 30 s, to the broadly peaked optimum value of $\delta\theta \sim \pi/2$ shown in the left-hand inset. Consequently, the experiment generally used $\pi/2 < \delta\theta < 2\pi/3$, meaning the
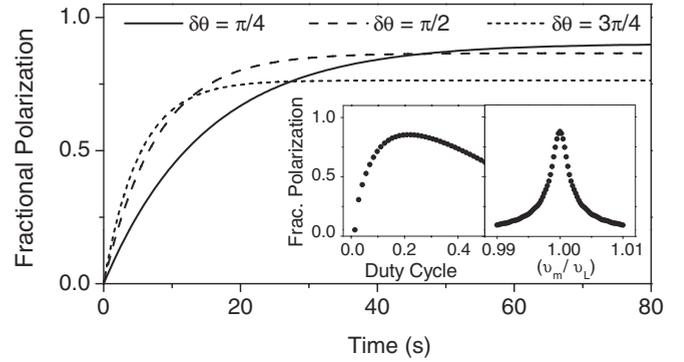

FIG. 2. Fractional atomic polarization P_A versus time for a range of modulation duty cycles $\delta\theta$. The curves were obtained by numerically integrating Eq. (4) with $\nu_m = \nu_L$ and per-atom pumping and relaxation rates of $\Gamma_p = 0.5$ s^{-1} and $\Gamma_r = 1/200$ s^{-1}, respectively. The left (right) inset gives, for the same Γ_p and Γ_r values and 30 s of optical pumping, P_A versus the modulation duty cycle for $\nu_m = \nu_L$ (P_A versus ν_m).

245-nm light was unblocked during 25%–33% of the pump phase.

Optimizing the pumping efficiency also requires precisely setting $\nu_m - \nu_L \sim 0$ (see the right-hand inset to Fig. 2); a 5% mismatch between the two frequencies, for example, reduces the equilibrium polarization by a factor of four. To meet this latter requirement, the pump light was modulated with an optical chopper whose on/off frequency was actively matched to the measured four-cell average Larmor frequency with a resolution limited only by the measured frequency itself. The chopper head was mounted on a pneumatic arm that moved the chopper and a quarter wave place out of the probe beam at the end of each optical pumping cycle (see Fig. 1).

The laser frequency was tuned 200 MHz below the $6\,^1S_0 \rightarrow 6\,^3P_1$ ($F = 1/2$) transition during the pump phase. At this detuning, the vector light shift due to the circularly polarized resonance light vanishes. This nulling does not occur exactly at the $F = 1/2$ line center due to the presence of the $F = 3/2$ hyperfine line. Controlling the pumping wavelength was also key to reducing Larmor frequency noise associated with light-shift-induced vertical magnetization of the ^{199}Hg vapor. This latter effect is detailed below.

B. Detection of Larmor precession

During the probe phase, the laser is detuned from the $6\,^1S_0 \rightarrow 6\,^3P_1$ ($F = 1/2$) resonance, attenuated by a factor of 10, and switched from circular to linear polarization. The precessing spins, via optical rotation synchronous with the Larmor frequency, induce oscillating rotations of the probe beam's polarization, with a rotation angle proportional to $\hat{k} \cdot \boldsymbol{P_a}$. For each cell, this oscillating angle was measured with a UV-sensitive photodiode placed after a Glan-Thompson linear polarizer oriented at an angle of $\sim\pi/4$ relative to the light polarization. The photodiode outputs were quasisimultaneously sampled by a DAQ system at a rate of 200 Hz; typical Larmor frequencies were $\sim$17 Hz.

Optical rotation of the linearly polarized light arises from the atomic spin-induced time dependence for $(n_+ - n_-)$,
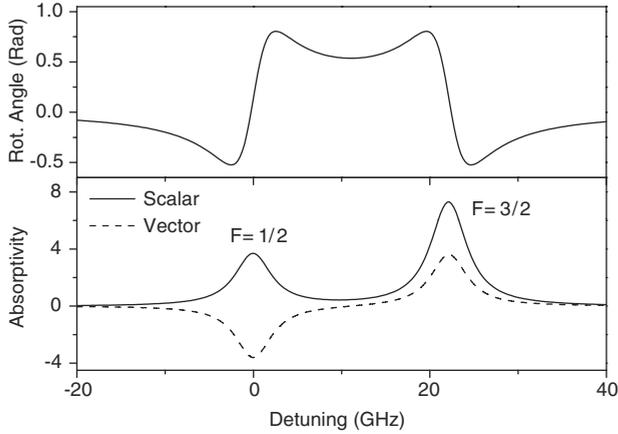
FIG. 3. Calculated optical rotation angle and scalar and vector absorptivity for ^{199}Hg as a function of detuning from the $6\,^1S_0 \rightarrow 6\,^3P_1$, $F = 1/2$ transition. The top (bottom) plot assumes 70% (full) atomic polarization and a propagation distance equal to the Hg vapor-cell diameter. All transitions are significantly pressure broadened by the buffer gas. The scalar absorption peaks for the $F = 1/2$ and $F = 3/2$ components are labeled by the excited-state hyperfine quantum numbers.

where n_+ and n_- are the indices of refraction for σ_+ and σ_- circularly polarized light, respectively: While the spin precesses at an angular frequency ω_L, the difference $(n_+ - n_-) \propto \sin(\omega_L t)$. The two equal-amplitude $\sigma_\pm$ components of the linearly polarized probe thus acquire a relative phase shift ϕ, where ϕ is given by $\phi = kl\mathrm{Re}(n_+ - n_-)$, where l is the propagation distance through the gas. In the linear polarization basis, this phase shift corresponds to a rotation of the plane of polarization by $\phi/2$. As shown below, differential absorption of the $\sigma_\pm$ components (which leads to elliptical polarization) was avoided in the experiment by tuning the probe to a frequency where the circular dichroism for the vapor vanishes.

Figure 3 shows the calculated optical rotation angle and the scalar and vector absorptivities for the $6\,^1S_0 \rightarrow 6\,^3P_1$ transition in ^{199}Hg as a function of detuning from the $6\,^1S_0 \rightarrow 6\,^3P_1$ ($F = 1/2$) hyperfine component. The scalar (vector) absorptivity encapsulates spin-independent (spin or $\sigma_\pm$ polarization dependent) absorption; the sum describes the total absorptivity for the vapor. The calculations were performed with the perturbative Ref. [11] formalism, wherein the ground-state Zeeman splitting is small compared to the transition linewidth, a criterion well satisfied by the experiment. Both plots use a room-temperature Hg saturated vapor density of 5×10^{13} cm^{-3}. Widths for the various features arise, for the 475 Torr of buffer gas used in the Hg vapor cells, primarily from the pressure-broadened linewidth of $\sim$4.5 GHz. Contributions to the optical rotation amplitude from the $F = 1/2$ and $F = 3/2$ lines (centered at 0 and 22 GHz, respectively) are equal, but have opposite signs, leading to the broadly peaked maximum midway between the lines.

Most of the Ref. [7] data used a probe light detuning of $+10$ GHz, or midway between the $F = 1/2$ and $F = 3/2$ lines. As shown in Fig. 3, this detuning optimizes the optical rotation amplitude while minimizing the scalar absorptivity, enabling detection of the precessing spins with a high signal-to-noise ratio. Moreover, the circular dichroism
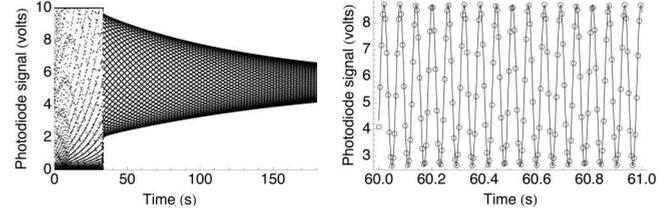

FIG. 4. Larmor precession signal. The raw signal is shown on the left. The detector is saturated during the initial 30 s of optical pumping. A 1-second magnification around 60.5 s is shown on the right. The signal noise is limited by the shot noise on the detected photons, giving a signal-to-noise ratio of about 3×10^4, although low-frequency magnetic gradient noise sets the noise floor of the experiment itself.

(or alternatively, the vector absorptivity) of the spin-polarized atomic vapor vanishes at this detuning. Therefore, the probe light remains linearly polarized despite the finite optical depth of the polarized vapor. This feature, in combination with the $\hat{k} \cdot \hat{b} = 0$ probe geometry, also suppresses Larmor frequency noise due to vector light shifts.

For typical running conditions, the observed optical rotation amplitude was $\sim$0.5 rad. The probe laser power was set to match the spin relaxation rate due to photon scattering to the rate of spin relaxation in the absence of light (i.e., it was set such that $\Gamma \simeq 2\Gamma_r$). For signals near the photon shot noise limit, this choice is equivalent to maximizing the sensitivity per unit time. The resulting spin coherence lifetimes were 100–200 s. A typical single-cell precession signal for an individual scan is shown in Fig. 4. The signal noise is limited by the shot noise on the detected photons, giving a signal-to-noise ratio that starts at $\sim 3 \times 10^4$ and decays to roughly half this value over the course of the scan.

C. The 254-nm laser

The 254-nm laser light is generated by frequency quadrupling the output of a commercial master-oscillator, power-amplifier (MOPA) semiconductor laser that operates at 1015 nm. A schematic for the laser is given in the inset to Fig. 1. The overall system design follows the prescription outlined in Ref. [12]. Additional details appear in Ref. [13].

A potassium niobate (KNbO$_3$) crystal in a bow-tie enhancement cavity first frequency doubles the infrared light to 508 nm. A second enhancement cavity with a β-barium borate (BBO) crystal then frequency doubles the light again to 254 nm. The entire system is enclosed in a Laminar flow hood equipped with a HEPA filter. Servos based on the Hansch-Couillaud scheme [14] actively lock the two doubling cavities to their respective inputs. At full power, the system produces 500, 100, and 6 mW of 1015-, 508-, and 254-nm light, respectively. The short-term linewidth for the 1015-nm laser is $<$1 MHz. The 254-nm power is actively stabilized via feedback to the drive current for the 1015-nm power amplifier. Under typical operating conditions, the measured 254-nm power noise lies within 30% of the photon shot-noise level in the sub-100 Hz bandwidth relevant to the experiment [15].

During a single experimental cycle, the 254-nm laser frequency is actively locked to (and flips between) the pump and probe detunings outlined above.

At both the pump and probe detunings, the laser frequency is stabilized by locking to the sides of absorption lines due to other Hg isotopes, using a reference cell containing Hg at natural isotopic abundance. The 1015-nm master oscillator's piezo-controlled diffraction grating is used to steer the 254-nm output.

With the reference cell locks engaged, in-loop analysis indicates that jitter and drift in the 254-nm laser frequency is <5 MHz.

D. Hg vapor cells

The Hg vapor-cell bodies were made from Suprasil cylindrical stock with a 2.54-cm outer diameter, a 0.159-cm wall thickness, and a length of 1.1 cm. Two Suprasil tubes (hereafter referred to as stems) with 3.3-mm outer diameters were attached to the cylindrical sections along their diameters. Two 0.159-cm-thick Corning 7980 fused silica optical flats with 3.81-cm diameters form the cell end caps. A conductive tin oxide (SnO_2) coating was deposited on the flats, which were attached to the cell bodies with a UV-curing low-outgassing optical adhesive (Norland Products NOA88). The cells contained a room temperature saturated vapor of isotopically enriched mercury (92% ^{199}Hg), as well as 475 Torr of carbon monoxide (CO) as a buffer gas. Dotriacontane wax [$CH_3(CH_2)_{30}CH_3$] was used as a wall coating. During cell construction, a small amount of Hg was condensed in one of the stems (enough that microdroplets of liquid Hg remain in the sealed cell at room temperature). The other cell stem is used as a reservoir for excess dotriacontane wax.

The tin oxide-coated end caps served as electrodes for application of the electric field. During the experiment, one interior face of a measurement cell was held at a potential of ± 10 kV, while the other was held at ground. Typical leakage currents at this potential were $\leqslant 1$ pA. For some of the vapor cells, the tin oxide coating extended only over the interior faces of the end caps, and a conductive pathway to the outer surfaces was established with conductive silver paint. For other cells, the tin oxide covered the entire surface of the end caps, making the silver paint unnecessary.

During the experiment the cell-holding vessel was frequently purged with either SF_6 or N_2 to remove atmospheric moisture and maintain high surface resistivity on the exterior cell walls. The wax wall coating improves the electric field uniformity inside the cells and does not appreciably affect the leakage currents [13]. The electric field in similar vapor cells was shown to be reversible to within ~1.5% by measurements of the quadratic Stark shift of the $6\,^1S_0 \rightarrow 6\,^3P_1$ transition [13].

When initially prepared, the cells had typical dark lifetimes of 100–400 s. The cell lifetimes degraded with time under exposure to light resonant with the $6\,^1S_0 \rightarrow 6\,^3P_1$ transition. The lifetime degradation resulted only from exposure to resonance radiation, and therefore the damage mechanism was identified as coating damage due to collisions with ^{199}Hg atoms in the $^3P_0$ metastable state [16]. CO efficiently quenches metastable atoms to the ground state, and cells using this buffer gas exhibited much slower lifetime degradation than older cells using N_2 or an N_2-CO mixture. The wall coatings were renewed between data sequences by melting and redistributing
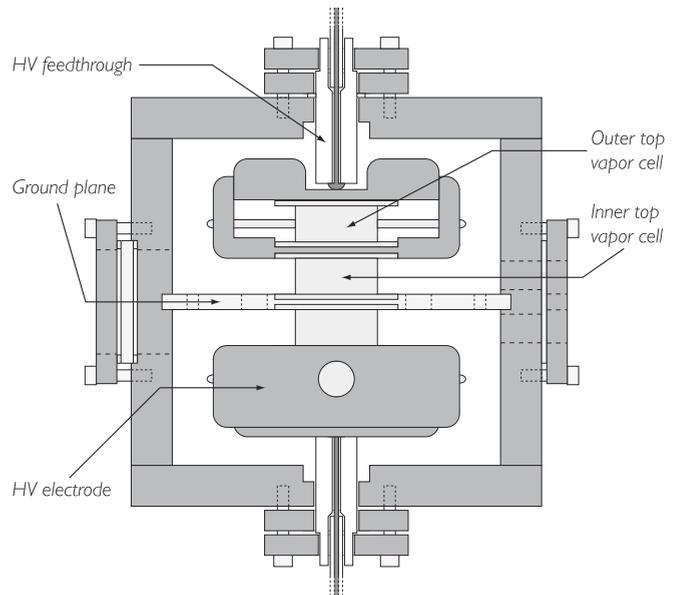

FIG. 5. Cutaway diagram of the cell vessel. Dark areas are conductive polyethylene, while the vapor cells are shown in gray. A stack of four vapor cells is visible; the outer bottom cell is shown inside its electrode, while for the outer top position the electrode has been cut away to reveal the cell.

the wax with a hand torch, which restored the cell dark lifetimes.

E. Cell vessel

The vapor cells were housed in a vessel constructed from graphite-filled UHMW polyethylene (TIVAR 1000 AntiStatic grade). This material has a specified surface resistivity of 10^5–10^9 Ω/square and a volume resistivity of 10^5–10^9 Ω cm and appears to be free of ferromagnetic impurities. Figure 5 gives a cutaway view of the vessel interior. The light beams entered the vessel through anti-reflection-coated fused silica windows and exited through anti-reflection-coated cylindrical collimating lenses that compensated for the defocusing induced by the curved vapor-cell walls. The vessel was purged with either SF_6 or N_2 gas to remove atmospheric moisture and outgassed material. Gastight seals were maintained through a combination of adhesive and gaskets hand made from Dow Corning 1184 pourable silicone rubber. The HV was brought into the vessel with RG-58 coaxial cable, and a HV feedthrough constructed from insulating TIVAR and a solder blob made the connection to the polyethylene electrode. The feedthrough contacts pressed on the electrodes, which pressed in turn on the measurement cells and maintained them in contact with the ground plane. Pressure was applied with a lip-and-collar system, adjustable with four nylon screws on the outside of the vessel. The feedthrough entrances were gas sealed with another collar that pressed on a silicone o-ring.

The electrodes that enclosed the outer cells were constructed from the same conductive polyethylene. The electrodes had four side holes arranged symmetrically around their circumference, two for light access and two that accommodated the cell stems. The electrode caps were secured with four nylon screws, and electrical contact between the cap

and the electrode body was maintained with dabs of custom silver paint. To reduce contact resistance, silver paint was also applied at the interface between the electrode and the HV feedthrough, and between the electrode and the adjacent measurement cell. All of the electrode exterior corners were rounded to help prevent field emission. For some electrodes, a small hand torch was used to flame polish the electrode surfaces to remove plastic hairs or other sharp surface features.

A fused silica ground plane divided the vessel into an upper and a lower half. The ground plane was constructed from three 0.159-cm-thick Corning 7980 fused silica plates that were glued together with the same optical adhesive used to assemble the cells. Indentations for the cell electrode discs and several through holes were laser cut into the silica plates. Each side of the ground plane was sputter coated with a Ti:W adhesion layer followed by a conductive Au film. The two conductive layers were isolated from one another so that leakage currents flowing across either of the two measurement cells could be separately collected. Wires attached near the four corners of the conducting film carried the leakage current out of the vessel where they connected to shielded cables through a resistor network.

F. High-voltage supply

The 10-kV power supply used to generate the static electric field was located in a separate room, approximately 12 m from the experiment. Two commercial power supplies were used over the course of the experiment. One was an all-solid-state model, while the other used a mechanical relay to switch the polarity of its output. The polarity-dependent magnetic field generated by this relay was large enough to be of concern as a possible systematic effect, and this supply was therefore shielded with a layer of high-permeability mu-metal. A separate computer was used to control the HV system and monitor any experimental parameters expected to explicitly depend on the applied electric field. To switch the polarity of the applied field, a (polarity-independent) digital signal was output from the main experiment computer and optocoupled to the HV control computer. The HV was transmitted over ~20 m of shielded RG8-U coaxial cable that was selected for its low dielectric leakage. Upon reaching the main room, the HV cable fed into a breakout box, where it was split into two smaller cables feeding the HV electrodes.

G. Leakage-current monitors

Leakage currents were continually monitored during the course of the experiment. The two sides of the vessel ground plane were isolated from one another, so that leakage currents from the top and bottom measurement cells could be separately collected and analyzed. We also monitored any current flowing onto the conductive cell vessel. These currents were brought to the HV DAQ system over shielded coaxial cables, where they were converted to voltages by an electrometer system before being sampled at 20 Hz and recorded by the computer. The system employed LMC6001 electrometer operational amplifiers with input currents of <25 fA and could resolve current fluctuations of 0.1 pA. The gain of the electrometer system could be switched under computer control, so that the
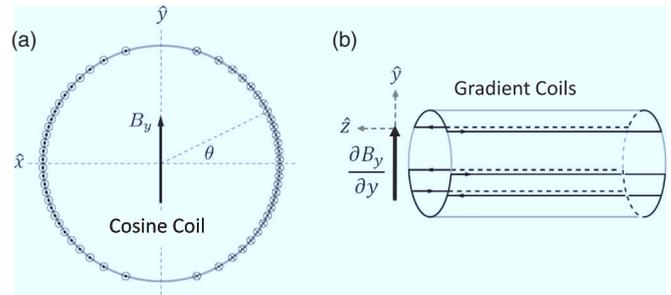

FIG. 6. Winding patterns for the (a) cosine and (b) gradient coils. In (a), the wires are distributed in a $\cos(\theta)$ pattern while (b) uses three single loops.

much larger currents that flowed during a change of the HV polarity could also be recorded.

H. Magnetic field generation and control

The 22-mG magnetic bias field was generated with a 15-turn cosine winding (see Fig. 6). The windings were attached to an aluminum cylinder located inside the innermost magnetic shield. This coil produced a vertically oriented field. A sine-distributed coil and a solenoidal winding provided additional fields along the two horizontal axes during the tipped-field runs described below. The coils were powered by an ultralow noise current source optimized for long-term stability. The current source, based on the Ref. [17] circuit design, employed a mercury battery as a voltage reference and was contained in a thermally isolated enclosure.

The first-order vertical field gradient produced by the cosine coil was roughly one part in 10^4. Three additional single-loop coils were affixed to the inside of the aluminum cylinder and were used to further reduce the field gradient to about a part in 10^6. These gradient coils were driven by three independent current sources which employed a single low-noise solid-state voltage reference. Figure 7 shows a typical frequency profile for the four Hg vapor cells in the vertical direction with and without the gradient coils. The bias field and the gradient fields were reversed periodically during the course of the experiment, using external DPDT switches. The direction of the main bias
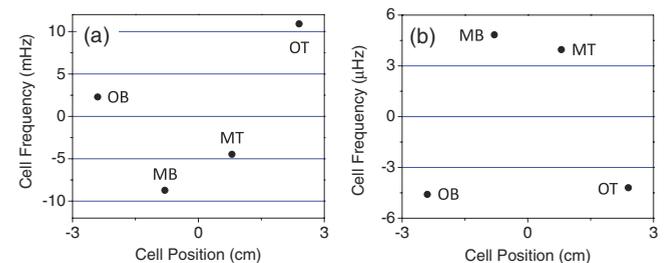
FIG. 7. (Color online) Typical four-cell frequency profile for (a) the cosine coil alone and (b) the cosine coil and the three single-loop gradient coils. Labels OT, MT, MB, and OB refer to the outer top cell, the middle top cell, the middle bottom cell, and the outer bottom cell, respectively. For both, the average frequency of ~17 Hz has been subtracted. Points are labeled by the corresponding vapor cells. Errors in the measured frequencies are smaller than the points. Note the factor of 1000 difference between the vertical axes for the two plots.
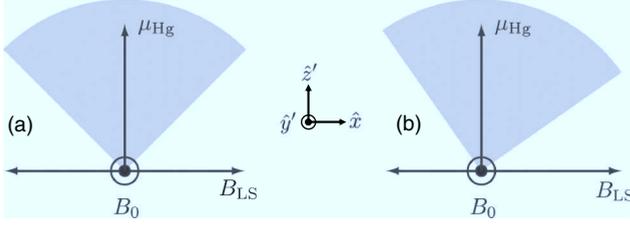
FIG. 8. In the rotating frame, the effective magnetic field B_{LS} generated by the pump light is normal to the main field B_0. In (a), the pump light modulation frequency (ν_m) matches the Larmor frequency (ν_L), so B_{LS} averages to zero over one precession period. In (b), $\nu_m \neq \nu_L$, leading to a nonzero average value for B_{LS}.

field was automatically logged at the start of each data run, and the degaussing procedure described below was employed after each field reversal.

The gradient coils were key to suppressing noise due to vertical magnetization, a process whereby fluctuating pump-phase vector light shifts lead to probe-phase Larmor frequency shifts. Figure 8 illustrates the basic effect. During the pump phase and in a frame that rotates at the Larmor frequency, the spin is stationary and oriented along the $\hat{z}'$ axis. The pump light $\hat{k}$ vector appears to rotate in this frame, sweeping out an angle determined by the light modulation duty cycle. Due to the spin dependence for the vector light shift, the circularly polarized pump shifts the $M_F = 1/2$ ($M_F = -1/2$) ground-state sublevel to higher (lower) energy; this effect can be treated as originating from a virtual magnetic field, $\boldsymbol{B}_{LS}$, oriented along the pump $\hat{k}$ vector with an effective strength proportional to the degree of pump light circular polarization. The component of $\boldsymbol{B}_{LS}$ which is transverse to the mean spin direction (B_{LS}) causes spin precession about the x' axis. If the modulation frequency ν_m matches the spin precession frequency, ν_L, the swept angle is symmetric about the spin in the rotating frame and B_{LS} averages to zero over one modulation period. If, however, $\nu_m \neq \nu_L$, the average light shift field does not vanish. Hence, B_{LS} will cause the spin to precess out of the x'-z' plane and onto the $\hat{y}'$ axis (i.e., the bias B-field axis).

For probe phase detunings away from the null points in the vector absorptivity (see Fig. 3), the circular dichroism of the polarized vapor induces circular polarization in the probe light as it traverses the cell, leading to a vector light shift whose magnitude is modulated at the Larmor frequency. The resulting virtual magnetic field causes the pump-phase vertical magnetization to rotate back onto the horizontal plane. The light shift field induced by circular dichroism always points along the spin; the rotated polarization, therefore, is perpendicular to the spin direction, leading to a phase shift of the precession signal given by $\delta\phi = P_{x'}/P_{z'}$, where $P_{x'}$ is [15]

$$P_{x'}(t) \sim \gamma t P_y(t)\langle B_{LS}\rangle = P_{x'}(0)(te^{-2\Gamma t}), \quad (8)$$

where $\langle B_{LS}\rangle$ denotes averaging over one modulation cycle and $P_{x'}(0) = \gamma P_{z'}(0)\langle B_{LS}\rangle$. The apparent frequency shift after a time t is then

$$\delta\omega(t) = \frac{\delta\phi}{t} = \frac{1}{t}\frac{P_{y'}(t)}{P_{z'}(t)} = \delta\omega_0(e^{-\Gamma t}), \quad (9)$$

where $\delta\omega_0 = P_{x'}(0)/P_{z'}(0)$.

In the absence of active control over the pump and probe beam frequencies, this effect (and the accompanying measurement time-dependent frequency drift) can easily produce shifts in excess of 100 nHz and thus become the dominant contribution to the scan-to-scan frequency noise. Moreover, the degree to which the effect can be eliminated is proportional to the overall frequency spread across the four-cell stack (or, alternatively, magnetic gradients across the stack) as this spread sets how well ν_m can be matched to the average Larmor frequency. Once identified, these issues were addressed via the gradient coils and active pump and probe frequency locks to the vector absorptivity nulls shown in Fig. 3 (see Refs. [15,18]). As indicated by Fig. 7, the former enabled a 1000-fold improvement in setting ν_m to the average Larmor frequency. With these measures in place, noise due to vertical magnetization lies well below the current long-term system noise floor.

I. Magnetic shielding

The Hg vapor cells were shielded from external magnetic fields by three cylindrical layers of Co-Netic AA high-permeability alloy. The cylinders had diameters of 30.5, 45.7, and 61.0 cm, and lengths of 53.3, 76.2, and 121.9 cm. Each cylinder was closed off with a Co-Netic AA end cap that was slip fit over the cylinder. The end caps had 7.6-cm-diameter holes for cable routing and optical access and smaller 3.2-cm-diameter holes along center lines perpendicular to the cylinder axes for further optical access. Silicone rubber glue was used to center the annealed shields inside of mounting rings. The 3-mm-thick glue joints reduced the mechanical stresses acting on the shields.

The transverse and axial shielding factors of the assembly were measured to be 5×10^4 and 1×10^4, respectively [15]. A degauss procedure was used each time the shield end caps were remounted to increase the internal field stability. To degauss, about 100 amp-turns of ac current was passed through wire loops that enclosed all three shield cylinders. The amplitude of the computer-generated ac waveform was slowly ramped down with a 5-min time constant. A frequency of about 5 Hz was found to produce the best results.

IV. DATA ACQUISITION AND ANALYSIS

A. Data acquisition

The currents output by the four photodiodes that monitored optical rotation were first amplified by transimpedance circuits and then sampled quasisimultaneously by the DAQ system at 200 Hz. The photodiode signals were monitored differentially (taking two DAQ input channels each). The relevant DAQ inputs were prefiltered by active low-pass circuits with corner frequencies of 100 Hz. The quantization noise of the 16-bit DAQ system was slightly smaller than the photon shot noise. Other experimental parameters, such as the ambient temperature, magnetic field coil currents, etc., were sampled at 200 Hz and then software down-sampled to 2 Hz by averaging 100-point sections of the 200-Hz waveforms.

A single Larmor frequency measurement typically required 180–230 s, including 30 s of optical pumping and 150–200 s of precession. A typical data run lasted 24 h and consisted of

several hundred Larmor frequency scans. The HV polarity was alternated between scans and was switched during the optical pumping phase. Occasionally, a HV reversal was skipped to guard against possible false signals at the scan frequency of $1/230$ s.

Several data runs together, using the same stack of four vapor cells, form a grouping which we term a sequence. Various experimental parameters were varied over the course of a complete sequence. In particular, roughly equal amounts of data were taken with the vertically oriented bias field pointing either up or down. The HV ramp rate was also typically varied between four values during the course of a sequence, and several runs in a sequence were dedicated to searching for systematic effects. At the start of each new sequence, we rearranged the order and orientations of the vapor cells or installed a different set of vapor cells.

B. Frequency combinations

In a two-cell EDM apparatus (see, for example, Ref. [8]) there is only one significant linear combination of cell frequencies: the difference between the two cells. This difference is insensitive to common mode changes in the bias field, but is proportional to linear and higher-order gradients. The four-cell apparatus utilized here removes this limitation by adding two additional cells that act as comagnetometers. This configuration provides a hierarchy of two-, three-, and four-cell frequency combinations. Some of these maximize the EDM sensitivity while simultaneously suppressing magnetic field noise up through second-order gradients, while others have reduced or no EDM sensitivity but provide spatially selective probes for magnetic and/or leakage current systematics. In the following, we briefly outline the most useful two-, three-, and four-cell combinations.

Taylor expanding the magnetic field about the median plane for the cell stack, the Larmor frequencies for the four cells are

$$\nu_{OT} = \frac{\mu}{h}\left(b_0 + 3lb_1 + \frac{9}{2}l^2b_2 + \frac{9}{2}l^3b_3\right),$$
$$\nu_{MT} = \frac{\mu}{h}\left(b_0 + lb_1 + \frac{1}{2}l^2b_2 + \frac{1}{6}l^3b_3\right),$$
$$\nu_{MB} = \frac{\mu}{h}\left(b_0 - lb_1 + \frac{1}{2}l^2b_2 - \frac{1}{6}l^3b_3\right),$$
$$\nu_{OB} = \frac{\mu}{h}\left(b_0 - 3lb_1 + \frac{9}{2}l^2b_2 - \frac{9}{2}l^3b_3\right),$$

(10)

where μ is the ground-state magnetic moment, h is Plank's constant, b_n is the nth derivative of the magnetic field evaluated at $y = 0$ (i.e., the median plane), and $y_i = \{+3l, +l, -l, -3l\}$ are the center positions for the cells along the vertical y axis. Subscripts on the left-hand side denote cell positions: OT is the outer top cell at $y = 3l$, MB is the middle bottom cell at $y = -l$, etc.; Eq. (10) leads to six two-cell, four three-cell, and two four-cell frequency combinations. Table I lists the most useful combinations along with their sensitivity to magnetic field gradients and an EDM.

The two pairwise differences, $\Delta\nu_m = \nu_{MT} - \nu_{MB}$ and $\Delta\nu_o = \nu_{OT} - \nu_{OB}$, are insensitive to fluctuations in the common-mode magnetic field b_0. For a nonzero EDM d,

TABLE I. Linear combinations of two-, three-, and four-cell precession frequencies. The second and third columns give the dependence of each combination on magnetic field gradients and an EDM. d is the EDM for ^{199}Hg. The subscript MT refers top the middle top cell, the subscript OB refers to the outer bottom cell, and so on.

Frequency combination	Magnetic	EDM
$\nu_{MT} - \nu_{MB}$	$\frac{\mu}{h}\left(2lb_1 + \frac{1}{3}l^3b_3\right)$	$\frac{2dE}{h}$
$\nu_{OT} - \nu_{OB}$	$\frac{\mu}{h}(6lb_1 + 9l^3b_3)$	0
$\nu_{MT} - \frac{1}{2}(\nu_{MB} + \nu_{OT})$	$\frac{\mu}{h}(-2l^2b_2 - 2l^3b_3)$	$\frac{3dE}{2h}$
$\nu_{MB} - \frac{1}{2}(\nu_{MT} + \nu_{OB})$	$\frac{\mu}{h}(-2l^2b_2 + 2l^3b_3)$	$-\frac{3dE}{2h}$
$\nu_{MT} - \nu_{MB} - \frac{1}{3}(\nu_{OT} - \nu_{OB})$	$\frac{\mu}{h}\left(-\frac{8}{3}l^3b_3\right)$	$\frac{2dE}{h}$
$\nu_{OT} + \nu_{OB} - (\nu_{MT} + \nu_{MB})$	$\frac{\mu}{h}(8l^2b_2)$	0

$\Delta\nu_m \propto 2dE/h$, while $\Delta\nu_0$ (derived from cells at zero electric field) has no EDM sensitivity and instead probes magnetic gradient noise. The two three-cell combinations trade reduced sensitivity to magnetic effects (both are independent to magnetic fields through first-order gradients) for reduced EDM sensitivity. The four-cell combination $\Delta\nu_c = (\nu_{MT} - \nu_{MB}) - \frac{1}{3}(\nu_{OT} - \nu_{OB})$ overcomes this limitation by recovering the $\Delta\nu_m$ EDM sensitivity while simultaneously eliminating magnetic field noise through second-order gradients. $\Delta\nu_{EDM}$ thus gives the best EDM sensitivity. Note the factor of $1/3$ in the definition for $\Delta\nu_c$ results from the 3-times-greater separation between the two outer cells compared to the middle cells. The final four-cell combination, $\Delta\nu_t = \nu_{OT} + \nu_{OB} - (\nu_{MT} + \nu_{MB})$, cancels magnetic noise through first-order gradients, but is insensitive to an EDM. This channel, therefore, provides the most sensitive monitor for magnetic systematic effects, particularly those generated by leakage currents.

C. Data analysis

During the probe phase, the optical rotation angle $A(t)$ is given by

$$A(t) = A_0\sin(\omega_L t + \phi)e^{-\Gamma t}. \tag{11}$$

The light intensity I registered by the Fig. 1 photodiodes is then

$$I(t) = I_0\sin^2[\alpha + A(t)], \tag{12}$$

where α is measured relative to the extinction point for $A = 0$, nonrotated light. In the limit of small optical rotation amplitude A, Eq. (12) becomes

$$I(t) = \frac{I_0}{2}[1 - \cos(2\alpha) + 2A\sin(2\alpha)\sin(\omega_L t + \phi)e^{-\Gamma t}], \tag{13}$$

which can be written more compactly as

$$I(t) = A_p\sin(\omega t + \phi)e^{-\Gamma t} + C, \tag{14}$$

where the generalized amplitude $A_p = AI_0\sin(2\alpha)$, the background $C = \frac{I_0}{2}[1 - \cos(2\alpha)]$, and ϕ is the signal phase.

In practice, nonlinearities in the small angle approximation of Eq. (12) and in the polarizer response distort the decay envelope and generate signal harmonics. The latter were
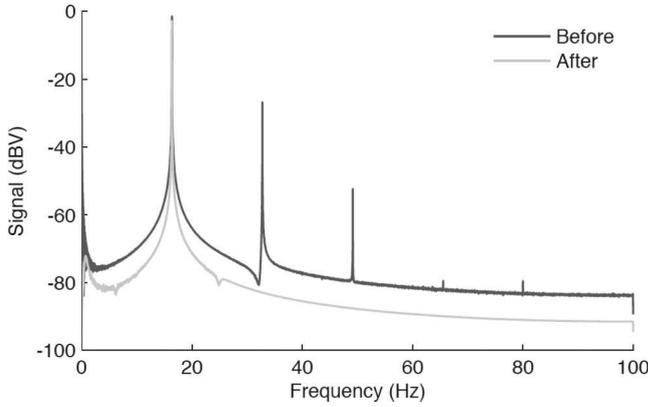
FIG. 9. Power spectra for a typical precession signal. The solid line gives the power spectrum for the data as initially acquired while the dashed line gives the spectrum for the same data after the frequency-space harmonic filtering and background removal described in the text.

removed with a frequency-space digital filter. The data were first transformed into frequency space with a fast Fourier transform (FFT) based on a split-radix algorithm [Duh84]. The Fourier transformed data was then multiplied by

$$F(f) = \frac{1}{e^{(f-f_c)/f_w} + 1}, \tag{15}$$

where f is the frequency, f_c is a cutoff frequency, and f_w defines the width of the crossover from $F \sim 1$ for $f \ll f_c$ to $F \sim 0$ for $f \gg f_c$. The filter width and cutoff frequencies were set to 0.1 and 25 Hz (or midway between the precession frequency and its second harmonic), respectively. The filtered data were then returned to the time domain by applying an inverse Fourier transform. Drifts in the data background were then removed by subtracting, in the time domain, a second filtered version of the data for which $f_c = 2$ Hz. This process effectively set C in Eq. (14) to zero. To avoid the edge effects that invariably result from applying Fourier filters to finite duration data, the first and last 5 s of the data were then dropped. Figure 9 shows a typical single-scan power spectrum before and after the filtering process. In the last four data sequences, the frequency-space digital filter was replaced by a digital notch filter that removed the constant term and the second and third harmonics of the signal. The filtered data point at time t_i, $S_f(t_i)$ was derived from the raw data points, $S(t_j)$, as follows:

$$\begin{aligned} S_f(t_i) = &\, S(t_i + 2\pi/3\omega) - S(t_i - 2\pi/3\omega) \\ &+ S(t_i + \pi/3\omega) - S(t_i - \pi/3\omega), \end{aligned} \tag{16}$$

where ω is the Larmor frequency. Raw data points were recorded at intervals close to $\pi/6\omega$; a small interpolation correction was used to account for the difference between $\pi/6\omega$ and the arrival time of the points. The notch filter did not require dropping the first and last 5 s of data. After the digital filtering, a Levenberg-Marquardt nonlinear least-squares routine was used to fit Eq. (14) to the filtered data, with ω, Γ, A_p, and ϕ as free parameters.

Errors for ω can be extracted from the fit covariance matrices. However, we instead used a phase deviation method that more accurately accounts for Larmor frequency drifts

within a single scan. After fitting the data over the entire fit range, the scan was divided into 100 equal-length sections ($i = 1, \ldots, 100$) that were each individually refit to Eq. (14), but with fixed ω and Γ (set by the overall fit) and A_p and ϕ free. The difference between ϕ_i for the shorter segments and the overall phase ($\phi_i - \phi$) then gives the phase deviation over the course of the scan. This deviation, in turn, provides a measure of the Larmor frequency stability during the probe phase. Note that since drifts in the Larmor frequency are most likely related to magnetic field drifts, the phase deviation can also be interpreted as the integral of the magnetic field inside the cell. Linear drifts in the magnetic field, for example, lead to quadratic drifts in the phase deviation.

For a given scan, $d\phi(t)/dt$ was next determined by fitting a straight line (via the least-squares method) to ($\phi_i - \phi$) versus time. Two items were extracted from the returned slopes. First, the central value for the slope was used as a correction, meaning the final value for the Larmor angular frequency was set equal to $\omega = \omega_0 + d\phi(t)/dt$.

Making this correction reduces frequency "pulling" by the earlier portion of the scan (when signal amplitude are larger), an effect which could bias cell frequency differences if the spin coherence times differ from cell to cell.

Second, the error in the slope, or $\delta[d\phi(t)/dt]$, was taken as the final Larmor angular frequency error for the scan. For linear frequency combinations such as $\Delta\nu_c = \Delta\omega_c/2\pi$, the phase deviations for the component cells were first combined (with appropriate signs and weighting) and then fit to straight lines.

The HV correlated components for each of the measured frequencies, combined frequencies, and monitored system parameters were then extracted with an n-point overlapping string analysis, a technique that removes slow data drifts while isolating any underlying HV correlations [19]. In the presence of a linearly drifting background, for example, combining successive frequency measurements with opposite HV polarity according to the three-point string:

$$s_i = \frac{\nu_i - 2\nu_{i+1} + \nu_{i+2}}{4}, \tag{17}$$

where ν_i is the measured frequency for scan i removes the linear drift and isolates the electric field correlated frequency shift s_i. For higher-order drifts, Eq. (17) generalizes to

$$s_i = \frac{1}{2^{n-1}} \sum_{m=0}^{n-1} (-1)^m \frac{(n-1)!}{(n-m-1)!(m)!} \nu_{i+m}, \tag{18}$$

where the uncertainty for s_i is given by

$$\sigma_{s_i} = \sqrt{\sum_{m=0}^{n-1} \left(\frac{1}{2^{n-1}} \frac{(n-1)!}{(n-m-1)!(m)!} \delta\nu_{i+m} \right)^2}, \tag{19}$$

where $\delta\nu_i$ is the error associated with ν_i. This approach is equivalent to removing an order $n - 2$ polynomial baseline from the data. To guard against uncorrelated signals at the scan-to-scan measurement frequency, HV reversals were occasionally skipped, with a corresponding truncation of the affected string. Although the data were often analyzed with three-, four-, five-, and six-point overlapping and nonoverlapping strings, three-point overlapping strings generally gave the
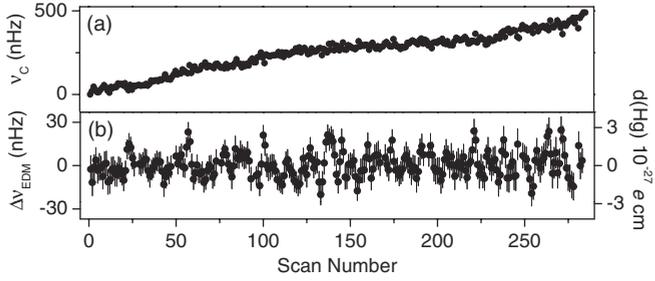
FIG. 10. (a) $\Delta\nu_c$ and (b) $\Delta\nu_{EDM}$ for a typical run. In (b), the reduced χ^2 is 1.2 and the run-averaged statistical error is 0.85 nHz after scaling by χ^2.

lowest scatter amongst string points and were thus used for the final data analysis.

For a given parameter with string points s_i, the run-averaged HV correlation was determined from the weighted mean:

$$\bar{s} = \frac{\sum \left[s / (\sigma_{s_i})^2 \right]}{\sum \left[1 / (\sigma_{s_i})^2 \right]}, \tag{20}$$

with an uncertainty

$$\sigma_{\bar{s}} = f_o \sqrt{\frac{1}{\sum \left[1 / (\sigma_{s_i})^2 \right]}} \sqrt{\chi^2}, \tag{21}$$

where f_o is a correction factor that accounts for the interdependence of overlapping strings

$$f_o = \frac{2^{n-1}}{\sqrt{\sum_{m=0}^{n-1} \left(\frac{(n-1)!}{(n-m-1)! m!} \right)^2}}. \tag{22}$$

For example, 3-point overlapping strings require $f_o = 4/\sqrt{6}$. Finally, $\sigma_{\bar{s}}$ was multiplied by the square root of the reduced χ^2 where $\chi^2 = \frac{1}{N} \sum (\frac{\bar{s} - s_i}{\sigma_i})^2$. This approach effectively scales the run-averaged error to match the scatter in the string points.

In the following, the EDM signal, $\Delta\nu_{EDM}$, was obtained from the HV correlated component of $\Delta\nu_c$ via the three-point string analysis described above. Figure 10 shows $\Delta\nu_c$ and $\Delta\nu_{EDM}$ for a typical run. In general, the run-averaged χ^2 for $\Delta\nu_{EDM}$ was between 1 and 2.

V. SYSTEM SENSITIVITY AND NOISE FLOOR

A. Short-term noise

An ultimate limit on the sensitivity of the current ^{199}Hg EDM search can be obtained by starting with the EDM–electric field interaction which shifts the precession frequency by $2dE/h$. Taking the difference between two measurements with antiparallel E doubles the shift, but for independent measurements with equal errors it also increases the noise by $\sqrt{2}$. Hence, an uncertainty $\delta\nu$ in the measurement of the frequency shift leads to an uncertainty:

$$\delta d = \frac{h \delta\nu}{2\sqrt{2} E}. \tag{23}$$

For N particles, the ideal shot noise uncertainty for a single measurement of the precession frequency at the end of a free precession time T is $\delta\nu = (2\pi\sqrt{N}T)^{-1}$. Repeating the

measurement t/T times in a total integration time t, $\delta\nu$ becomes $\delta\nu(t) = (2\pi\sqrt{NTt})^{-1}$. A lower bound for δd, based on atom shot noise alone, is thus

$$\delta d = \frac{\hbar}{2E\sqrt{2NTt}}. \tag{24}$$

The vapor cells contain roughly 10^{14} atoms, and typically $T \sim 150$ s. With an electric field strength of 10 kV/cm, Eq. (24) predicts $\delta d \sim 7 \times 10^{-31}$ e cm or $\delta\nu \sim 6 \times 10^{-12}$ Hz for $t = 24$ h. The highest sensitivity runs in our EDM data set (Sec. VI) have 24-h uncertainties of $\sim 7 \times 10^{-10}$ Hz, 100 times worse than the atom shot-noise estimate. Estimates based on Eq. (24) are commonly employed as figures of merit for comparing different EDM experiments, although other noise sources often limit the attainable sensitivity to much more modest values.

The shot noise sensitivity of the ^{199}Hg experiment is significantly less than that given by Eq. (24) because (1) the atoms undergo spin relaxation during the measurement time T, (2) the signal is sampled uniformly throughout the measurement time rather than at the beginning and end of the precession period, and samples from the middle of the precession period do not determine the signal frequency as effectively as those at the beginning and end, (3) the amplitude of the sinusoidal signal is typically less than the dc level, so that the shot-noise limited SNR is less than ideal. The on-resonance optical depth of our cells is ~ 3, and we estimate that the detection quantum efficiency is about 20% (including losses at the cell exit surfaces and miscellaneous optics), so that we expect photon shot noise to dominate over atom shot noise [20]. The shot noise limit for extracting the frequency of an exponentially decaying sine wave is given by

$$\sigma_\nu^2 = \frac{6n^2(e^{2\Gamma T} - 1)}{4\pi^2 \Gamma A^2 T^4}, \tag{25}$$

where Γ is the decay rate of the sine wave, A is the initial amplitude of the wave, and n is the rms noise spectral density amplitude at the frequency of the wave. This equation may be compared to Eq. (11) of Ref. [21]. Equation (25) contains an additional factor $(e^{2\Gamma T} - 1)/\Gamma T$ which accounts for the decay of the signal amplitude at a rate Γ. Both equations assume all samples are weighted equally, as was done for the analysis of our experiment. Inserting typical numbers for the present experiment, $1/\Gamma \sim 100$ s, $T = 150$ s, $A = 3$ V, and $n = 20$ μV/$\sqrt{\text{Hz}}$ (the photon shot noise), $\sigma_\nu \sim 5.1 \times 10^{-9}$ Hz for each free decay. Taking the appropriate frequency differences between cells to extract the EDM, this uncertainty translates to $\delta\nu \sim 3.8 \times 10^{-9}$ Hz per free decay. In a 1-day run, there are ~ 400 separate free decays, leading to a shot noise estimate for the EDM sensitivity of $\delta\nu \sim 1.9 \times 10^{-10}$ Hz per day. For our recent EDM data set described below, data runs shorter than a day and excess noise resulted in an average per-run EDM sensitivity of $\sim 1.2 \times 10^{-9}$ Hz.

Figure 11 shows the angular frequency errors versus T for a typical scan along with the Eq. (25) prediction. The single-cell frequency error deviates from Eq. (25) after ~ 40 s due to the onset of magnetic field noise. The middle cell angular frequency difference, $\omega_{MT} - \omega_{MB}$, removes the common-mode magnetic noise and agrees well with the form of Eq. (25). However, the curve in Fig. 11 uses the measured rms noise $n = 30$ μV/$\sqrt{\text{Hz}}$ rather than the photon shot noise
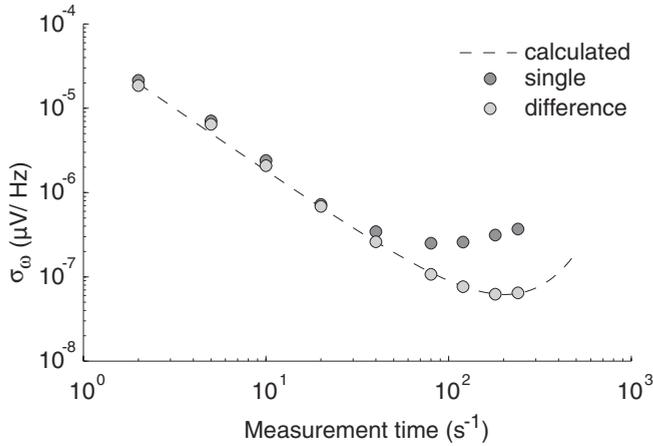
FIG. 11. Scaling of the single scan angular frequency error versus measurement interval, T. Each point is the average of the error from 100 single scans. For this run, the spin coherence times of the middle top (MT) and middle bottom (MB) cells were 100 and 160 s, respectively.

$n = 20 \ \mu\text{V}/\sqrt{\text{Hz}}$. The 50% excess arises from residual laser intensity noise.

B. Long-term noise

Over the course of a multihour data run, the scatter in $\Delta\nu_{\text{EDM}}$ was typically 1.5 times larger than expected from the individual scan uncertainties, indicating the presence of nonstatistical noise on the $\sim$200-s time scale between successive scans. Two noise sources were dominant: fluctuating magnetic field gradients due to the thermal motion of charge carriers (Johnson current noise) in the aluminum coil form and fluctuating vector light shifts due to imperfections in aligning the probe beam $\hat{k}$ vectors normal to the B-field coupled with variations in the probe beam frequency and residual circular polarization.

The low-frequency magnetic field noise on the axis of an infinitely long aluminum cylinder due to Johnson current noise is given by [22,23]

$$\delta B_J = \frac{\mu_0 \sqrt{t}}{4R}\sqrt{3k_B T \sigma}, \qquad (26)$$

where σ is the electrical conductivity of aluminum, R is the cylinder radius, and t is the thickness of the cylinder walls. For our aluminum coil form, $\delta B_J \sim 2.3$ nG Hz$^{-1/2}$. This field is amplified by a factor of 4/3 by the innermost magnetic shield, and when integrated over a 200-s interval leads to a scan-to-scan average precession frequency fluctuation of 170 nHz.

We expect that nth-order magnetic field gradient noise is suppressed by $(a/R)^n$ (where a is the gradiometer baseline), and the four-cell frequency difference channel $\Delta\nu_c = \nu_{MT} - \nu_{MB} - \frac{1}{3}(\nu_{OT} - \nu_{OB})$ (see Table I) is unaffected by gradient fields of up to second order. Taking the gradiometer baseline to be the separation between the outermost two cells, $a/R \approx 0.5$, the third-order gradient of the Johnson current noise was likely the dominant magnetic noise source for $\Delta\nu_c$. Other sources of magnetic field noise, such as external field fluctuations, coil current fluctuations, or noise arising from the innermost

magnetic shield were all either measured or estimated to be small.

The aluminum coil form has since been replaced by an epoxy resin coil form to reduce the Johnson current noise.

While taking data at different probe light intensities to investigate possible systematic errors, we observed that the daily precession frequency noise scaled roughly linearly with the probe light intensity, at odds with the expectations from Eq. (25). We attribute this excess noise to fluctuations of a vector light shift, whereby circularly polarized light produces a pseudomagnetic field along the wave vector, $\hat{k}$, of the probe light. Although the probe light was linearly polarized before entering the vapor cells, birefringence in the cell walls produced circular polarization amplitudes of $\sim$7% for the probe light within the cells. The $\hat{k}$ vector for each beam was nominally perpendicular to the precession magnetic field, but misalignments at the level of 3 mrad projected small components of the light shift fields along the precession field. Finally, between scans the UV laser frequency was shifted by 10 GHz and back, requiring laser cavity relocking. Small changes in the probe beam frequency, pointing, or degree of circular polarization within the vapor cells after cavity relock caused fluctuations in the projection of the light shift field along the precession axis, leading to frequency noise proportional to the probe light intensity. After the EDM data set was acquired, we improved the alignment of the $\hat{k}$'s relative to the precession field by a factor of ten and observed a fivefold reduction in the daily precession frequency noise for high probe beam intensity data runs. Scaling to the intensities used for EDM data, light shift noise was likely a dominant noise source.

VI. THE EDM DATA SET

Typical data runs spanned $\sim$24 h and utilized several hundred HV reversals. For a single run, the statistical error for $\Delta\nu_{\text{EDM}}$ was determined from the weighted error of the mean multiplied by the square root of the reduced χ^2 (typically, the reduced χ^2 was between 1 and 2). Nine separate vapor cells, four electrodes, two cell vessels, multiple permutations of the vapor cell and electrode orientations, and various configurations of the photodiode data-acquisition (DAQ) channels were used over the course of the measurement. Component changes were made between groups of 10–20 runs termed sequences; between successive sequences, the paraffin inside each cell was melted and the outer surfaces of the cells were thoroughly cleaned. The cells were also soaked in hydrochloric acid to remove any lingering ferromagnetic contaminants. Flips involving the vapor cells, electrodes, and vessels used nominally identical components. Each sequence included a roughly equal number of EDM-sensitive dipole HV runs ($+$ - $+$ - HV sequence) for the two main B-field directions and several runs targeted at systematic effects. Within a sequence, the HV ramp rate was permuted between 4, 2, 1, and 0.67 kV/s on adjacent runs. A limited number of dipole HV runs (eight total) were taken at 7 and 5 kV.

Data runs aimed at systematic effects focused on $|E|$-dependent shifts (explored via $+$ 0 - 0 quadrupole HV reversals) and $\boldsymbol{v} \times \boldsymbol{E}$ motional B-field effects (explored via dipole HV runs with the main B-field tipped by $\pm 10°$ along the
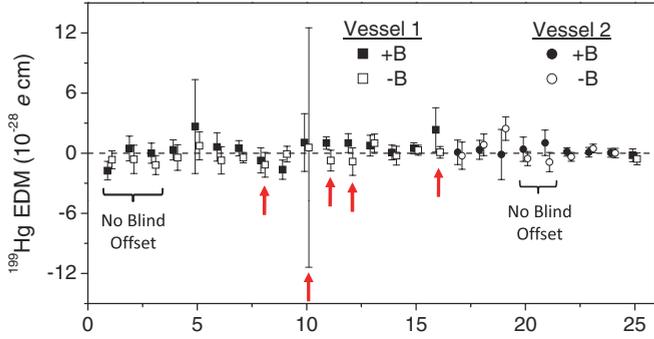
FIG. 12. (Color online) ^{199}Hg EDM versus sequence number. The error bars are statistical. Open (solid) symbols denote $+B$ ($-B$). Squares (circles) denote vessel 1 (vessel 2). The no-blind and arrowed sequences were excluded from the final analysis. The latter were dropped due to the apparent spark correlation described below.

middle and outer light beam $\hat{k}$ vectors). The latter were termed TF runs. The quadrupole HV runs were also analyzed for EDM-like frequency shifts by comparing dwells with positive HV polarity to dwells with negative HV polarity.

In an effort to remove experimenter bias, the EDM signal was concealed with a numerical blind during data collection and analysis. The blind comprised EDM-mimicking equal-magnitude (but opposite sign) frequency offsets that were added to the extracted Larmor frequencies for the two middle cells. The blind was constant within a given sequence; the final four sequences each used independent blinds. Each blind was selected with a random-number generator and stored in a binary file to avoid accidentally revealing the blind. The allowed range for the blinds was ± 0.8 nHz. This range was large enough to exceed the anticipated EDM sensitivity and the 2001 EDM limit [8], but small enough to reveal known sources for gross systematic error. During the final round of systematic error analysis, all of the sequences were analyzed with a single blind. This final blind was revealed only after the data cuts and error analysis were complete.

The raw EDM data set consisted of 278 runs spread across 25 sequences. Figure 12 shows the resulting sequence-level $+B$ and $-B$ values for $d(^{199}\text{Hg})$, where each was determined from the weighted average of the relevant runs for the two B-field directions. Within each sequence, the $+B$ and $-B$ EDMs are in good agreement. The data-set-wide $+B$ and $-B$ EDMs (taken as weighted averages over runs without regard to sequences) also agree within 1-σ. Systematic effects that flip sign relative to the EDM signal when B is reversed would appear in the difference, but cancel in the average of the $+B$ and $-B$ results. Although the data are apparently free of such problems, we conservatively determined sequence-level EDMs from straight averages of the $+B$ and $-B$ results.

Five sequences were acquired without a blind offset: three before the offset was implemented and two at high light intensity, with the latter used to set limits on intensity-dependent shifts. All five unblinded sequences were excluded from the final value for $d(^{199}\text{Hg})$. As detailed in Sec. VII C, an additional five sequences (arrowed in Fig. 12) were also excluded due to evidence for a potential correlation between the measured EDM and the number of microsparks per scan. The final EDM data set then comprised 166 runs acquired in 15 sequences. The

central $d(^{199}\text{Hg})$ value, obtained from the weighted average of these 15 sequence values was $d(^{199}\text{Hg}) = (0.49 \pm 1.29_{\text{stat}}) \times 10^{-29}\ e$ cm. This statistical error corresponds to a 0.1-nHz frequency difference between the two middle cells, or a $4\times$ improvement on Ref. [8].

With individual run errors set as outlined above, the reduced χ^2 for the 166 runs is 0.65. If, however, the runs are divided into ~ 3-h segments and the rest of the analysis is unchanged, we find $\chi^2 \sim 1$. Low-frequency drift that averages faster than white noise could account for this behavior. Such drift could arise, for example, from changes to the laser beam pointing that are coupled to the ~ 3-h time scale for resets of the piezoactuated doubling cavity mirrors.

VII. SYSTEMATIC EFFECTS

As detailed in Ref. [7], we did not find evidence for statistically significant correlations between $\Delta\nu_{\text{EDM}}$ and the vapor cells or electrodes (or their orientation inside the vessel), the DAC channel ordering, or the vessels. Moreover, the $\Delta\nu_{\text{EDM}}$ values extracted from the tipped B-field runs, the quadrupole HV runs, the high laser intensity runs, and the two-cell difference MD = $(\nu_{MT} - \nu_{MB})$ all agree with the Ref. [7] final central value at the 1-σ level.

Any remaining, EDM-mimicking systematic effects must satisfy two criteria: a correlation with the applied HV polarity and the production of frequency shifts that are asymmetric between the two middle vapor-cell positions. Table II summarizes the systematic errors for the various processes that meet these criteria. In the following, each one is described in detail.

A. Leakage currents

The electrical currents that flow during application of the HV electric field generate magnetic fields that can, under certain conditions, lead to HV-correlated shifts of the Larmor precession frequency. The size and direction for these leakage-current generated magnetic fields depends on the (unknown) details of the current paths, but to first order, only helical paths within or on the vapor-cell walls generate EDM-mimicking signals for the magnetic and electric field geometry used here.

Figure 13 shows a scatter plot of the run-level $\Delta\nu_{\text{EDM}}$ versus the middle top cell leakage current. A linear fit to this data gives a correlation slope of (-56 ± 450) pHz/pA. Similarly, scatter plots of $\Delta\nu_{\text{EDM}}$ versus the middle bottom cell and vessel leakage current string points give correlation slopes of (-6 ± 560) and (1 ± 30) pHz/pA, respectively. All three correlations are unresolved. The corresponding correlation probabilities, obtained from standard linear

TABLE II. Systematic error budget ($10^{-30}\ e$ cm).

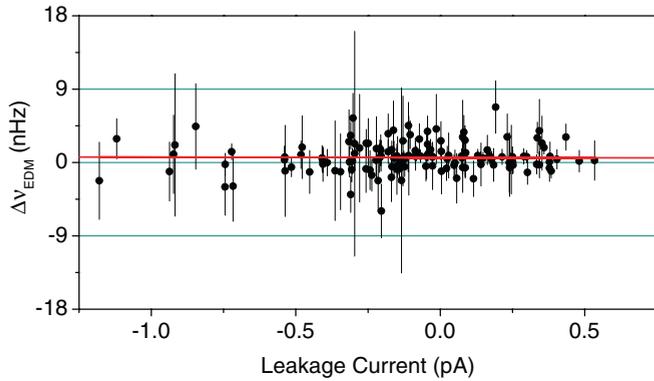| Source	Error	Source	Error
Leakage currents	4.53	Charging currents	0.40
Parameter correlations	4.31	Convection	0.22
Spark analysis	4.16	($\boldsymbol{v} \times \boldsymbol{E}$) B-fields	0.15
Stark interference	1.09	Berry's phase	0.02
E^2 effects	0.62		
	Quadrature sum 7.63		

FIG. 13. (Color online) Run-level $\Delta\nu_{EDM}$ versus the measured middle top cell leakage current. The solid line is a least-squares, straight-line fit. The leakage currents are sometimes negative, an effect we attribute to capacitance changes caused by charge redistribution on nearby insulators.

regression of the same data, are 13%, 1%, and 8%, respectively. The resulting leakage current systematic error, obtained by combining the average leakage current of 0.42 pA with the largest 1-σ correlation limit (given by $\Delta\nu_{EDM}$ versus the middle bottom current) is 2.7×10^{-29} e cm. Note, however, that this estimate is inflated by the large uncertainty for the unresolved correlation itself which, in turn, is largely set by the relatively small span for the current. In addition, the correlation analysis assumes that the leakage currents that change from run to run project onto an EDM in the same way as any residual leakage current does.

A more realistic estimate for the leakage current systematic error can be obtained by examining the leakage currents and their possible paths in greater detail. As shown in Fig. 14, the leakage currents display two qualitatively different behaviors: The first, termed gas currents because they flow through the vessel gas exterior to the cells, scale with the purge gas age when the gas is periodically refreshed, while the second, termed baseline currents, persist after the purge gas is refreshed or when the gas flows continuously.

After EDM data taking had ended, the vessel ground plane was modified to allow independent measurements of
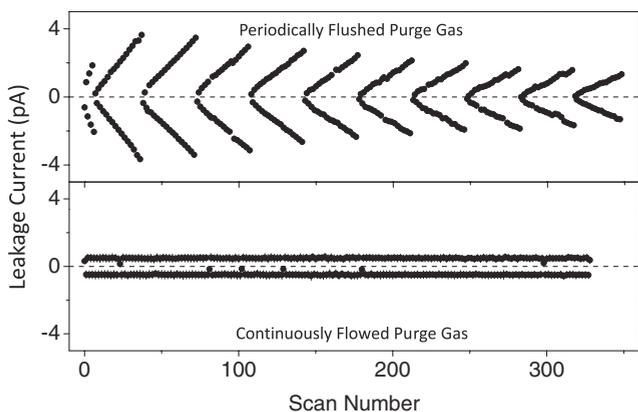

FIG. 14. The top (bottom) panel shows typical leakage currents for the middle bottom vapor cell when the purge gas is periodically flushed (continuously flowed).

the leakage currents that flowed to the cell end-cap disk and to the neighboring vessel ground plane. It was found that more than 80% of the total leakage current flowed to the vessel ground plane, and not down the cells walls. As the purge gas rate was reduced, the leakage current to the vessel ground plane increased, as in Fig. 14. Because the gas currents follow the local electric field lines, any helical component to the gas current is negligible. In the following, therefore, we focus on the baseline currents.

The baseline current has contributions from currents flowing in the interior of the cell, through the bulk of the fused silica cell walls, on the outer cell wall surface, and residual currents flowing through the dry gas exterior to the cell. Both the residual exterior gas currents and currents interior to the cells lack coherent helicity since the wax that coats the inside of the cell walls is remelted each sequence. It is more difficult to quantify the paths that currents flow in the bulk of the cell walls and on the outer cell wall surface. However, the two opposed cell stems break the cylindrical symmetry of the cell walls. Attaching the cell stems also adds local impurities to the fused silica and a local thickening of the cell wall, both leading to a reduced bulk resistivity. Exterior to the cell, the cell stems modify the local electric fields. A conservative model for helical current flow, therefore, is 1/2 of a full turn around the cell body before the current finds a lower-resistance path to ground near one of the two cell stems.

Given the 1.25-cm cell radius, a full turn of current around a cell wall creates a magnetic field at the cell center of $B_L = 0.5$ pG/pA. At the adjacent cell center, 1.6 cm away, the field is reduced to $0.23B_L$. The resulting frequency shift in the $\Delta\nu_{EDM}$ channel is then approximately 0.27 nHz/(pA-turn). The average single-cell leakage current was 0.42 pA. The fields in the two middle cells can either add or subtract, so we take $\sqrt{2} \times 0.42$ pA = 0.59 pA as the effective current. The EDM data set employed nine different vapor cells (four dominate the final statistical error) whose helical current paths should be uncorrelated. To account for this averaging, we divide by 2. Combining the above gives the Table II systematic error of 4.53×10^{-30} e cm. Note, this estimate assumes that all of the measured current flows in a helical path of 1/2 of a full turn. More recent measurements indicate that it is likely that at least 80% of this current was residual current that flowed through the gas.

Ground-plane currents are also a potential source for systematic shifts. In the unlikely scenario of a preferred current path down one side of a cell and then out to an opposing corner of the ground plane, the current will follow the lowest-resistance path to the corner and may favor looping around one side of the cell (if, for example, the relevant conductive pathway is shorter or the nearer side of the ground plane contains scratches). Ground-plane currents, however, produce fields that are nearly matched in the two middle cells. At a ground plane path radius of 2 cm, for example, the fields in the middle cells are equal to within 20%, leading, for 1/2 turn, to HV correlated magnetic fields that are 2$\times$ smaller than the fields resulting from helical flow around the cell walls. Moreover, this process relies on a fortuitous alignment of defects in a given vapor cell and ground plane. It is thus unlikely to produce coherent systematic shifts that survive the multiple cell changes, permutations of the cell orientations, and

TABLE III. Parameter correlation systematic error. Parameter descriptions are given in the text.

Parameter	Feedthrough (pHz)	d (10^{-30} e cm)
Middle lifetime	-0.22 ± 1.67	0.22
Outer lifetime	-0.50 ± 1.20	0.19
Middle amplitude	1.95 ± 2.18	0.47
Outer amplitude	0.80 ± 1.32	0.24
Middle transmission	0.85 ± 0.61	0.13
Outer transmission	0.13 ± 1.68	0.21
PhDev middle	-0.002 ± 0.02	0.002
PhDev outer	0.002 ± 0.01	0.002
Ambient Bx	1.61 ± 4.75	0.72
Ambient By	0.01 ± 0.21	0.03
Ambient Bz	1.28 ± 4.20	0.62
Cavity piezo 1	0.74 ± 4.17	0.56
Cavity piezo 2	0.08 ± 0.45	0.06
245-nm power	1.57 ± 3.00	0.52
IR laser current	5.35 ± 6.74	1.01
UV frequency lock	0.29 ± 0.79	0.12
UV feedforward	1.78 ± 3.03	0.55
Grad coil 1	8.07 ± 14.71	1.94
Grad coil 2	0.30 ± 2.28	0.29
Grad coil 3	1.46 ± 5.07	0.74
Main coil	19.11 ± 19.68	3.29
Quadrature sum		4.31

use of two separate ground planes employed for the Fig. 12 data.

B. Parameter correlations

The parameter correlation systematic error accounts for the possibility of generating false EDMs via correlations between $\Delta\nu_{EDM}$ and a given experimental parameter (such as the UV laser power) and, in parallel, accidental correlations between the same parameter and the HV electric field. To account for this possibility, a frequency error feedthrough, $c \pm \Delta c$, was calculated for each of the monitored fit and system parameters. Here, $c \pm \Delta c = (a \pm \Delta a)(b \pm \Delta b)$ where a and Δa are the central value and error for the HV correlation of a given parameter and b and Δb are the central value and error for the correlation of the same parameter with $\Delta\nu_{EDM}$. The latter are based on least-squares, straight-line fits of the $\Delta\nu_{EDM}$ string points versus the string points for a given parameter. Specific parameters include: the vapor-cell spin amplitudes, lifetimes, relative phases, and UV transmission; the laser power, frequency, drive current, and doubling cavity piezo control voltages; an external three-axis flux gate magnetometer that monitors the ambient magnetic field; and the B-field coil currents (the main coil and three gradient coils). Possible systematic errors due to the HV charging and leakage currents are treated elsewhere.

Table III summarizes the individual parameter correlation errors. To avoid double-counting, composite values were determined for the outer and middle vapor-cell lifetimes, amplitudes, and transmission where, in each case, the Table III values are the error-propagated mean feedthrough for the two relevant vapor cells. As shown, no statistically significant correlations were found; note intermediate values, $a \pm \Delta a$ and
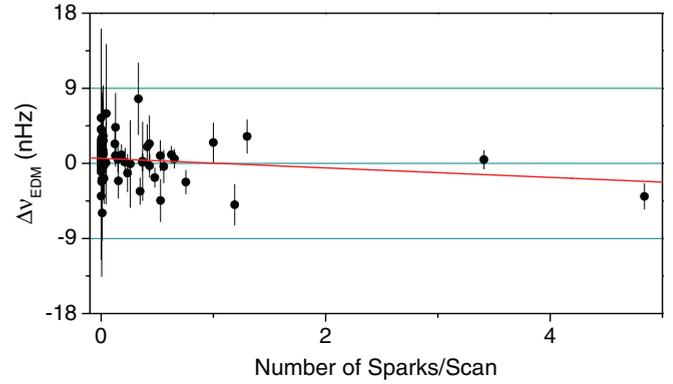

FIG. 15. (Color online) Run-level $\Delta\nu_{EDM}$ versus the number of sparks per scan for the middle top vapor cell. The solid line is a least-squares linear fit.

$b \pm \Delta b$, are similarly unresolved. Consequently, $c \pm \Delta c$ for each parameter was converted into a 1-σ upper limit $|c| + \Delta c$, given in EDM units in the right-most column. The largest value, from the main coil channel, is 3.29×10^{-30} e cm, or a factor of four smaller than the EDM statistical error of 1.29×10^{-29} e cm. Combining all of the Table III entries in quadrature gives the Table II parameter correlation systematic error of 4.31×10^{-30} e cm.

C. Sparks

Microsparking between the HV electrodes and the ground plane or the vessel walls can lead to EDM-like systematic errors via several processes including magnetizing trace ferromagnetic impurities, altering the magnetization of the magnetic shields, inducing charge accumulation that may create forces on the cells, or directly generating magnetic fields with projections along the main B-field axis. In the experiment, microsparks are logged as short-duration, >100 pA spikes in the continuously monitored leakage currents. Greater than 99% of the sparks observed occurred in the five excluded sequences during which the vessel was periodically flushed with N_2 (see Fig. 12).

Figure 15 is a scatter plot of run-level $\Delta\nu_{EDM}$ versus the number of sparks per scan for the middle top vapor cell. A linear fit to this data gives a correlation slope of (-0.57 ± 0.22) nHz/spark. Similar scatter plots of $\Delta\nu_{EDM}$ versus the number of sparks per scan for the middle bottom cell and the vessel give correlation slopes of (-0.12 ± 0.47) nHz/spark and (0.58 ± 0.71) nHz/spark, respectively. The corresponding correlation probabilities, determined from standard linear regression of the same data, are 99%, 20%, and 55%, respectively. This analysis is compromised by the relatively small number of measurements at the highest spark rates. The total current carried by the sparks creates magnetic fields that are insufficiently large, even for unity projection along the main B-field, to generate correlation slopes at the level of of (-0.57 ± 0.22) nHz/spark, but other mechanisms such as those mentioned above could still lead to an electric-field-correlated frequency shift.

Two approaches to removing the apparent spark correlation were applied to the EDM data set. The first approach cut individual scans with sparks while the second cut entire
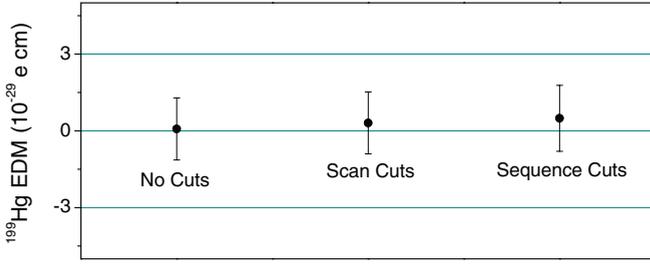
FIG. 16. (Color online) $\Delta\nu_{\text{EDM}}$ without spark cuts compared to $\Delta\nu_{\text{EDM}}$ obtained with scan and sequence-level spark cuts. The error bars are statistical. Central values for the two cutting schemes agree to within 1.8×10^{-30} e cm. The maximum shift in $\Delta\nu_{\text{EDM}}$ with and without spark cuts is $<4.2 \times 10^{-30}$ e cm.

sequences containing sparks. As shown in Fig. 16, the central values for the two spark cutting schemes agree to within 1.8×10^{-30} e cm. The maximum shift in $\Delta\nu_{\text{EDM}}$, obtained by comparing the sequence-elimination approach to the original data set, is $<4.2 \times 10^{-30}$ e cm. We adopted the more conservative sequence-elimination central value. A spark analysis error equal to the resulting $\Delta\nu_{\text{EDM}}$ shift (i.e., 4.2×10^{-30} e cm) was then assigned to reflect the possibility that the spark correlation was a statistical aberration.

D. Stark-induced interference

The HV electric field couples opposite parity states to the $6\,^1S_0$ ground-state and the $6\,^3P_1$ excited-state (hyperfine components $F = 1/2$ and $F = 3/2$), resulting in the familiar quadratic Stark shift. Coupling opposite parity states also causes the $6\,^1S_0 \rightarrow 6\,^3P_1$ transition to acquire magnetic dipole ($M1$) and electric quadrupole ($E2$) components in addition to its normal electric dipole ($E1$) amplitude. The $M1$ and $E2$ amplitudes can interfere with the $E1$ amplitude, producing an EDM-mimicking vector light shift that is linear in the applied electric field. This Stark interference effect was first predicted [24] and measured [25] in the context of a Rb EDM experiment. The effect has also been calculated for ^{199}Hg [26,27].

Stark interference leads to a small fractional change in the absorptivity α of the $6\,^1S_0 \rightarrow 6\,^3P_1$ transition

$$\frac{\delta\alpha}{\alpha} = (a_{M1} + a_{E2})(\hat{\epsilon} \cdot \boldsymbol{E})(\hat{k} \times \hat{\epsilon}) \cdot \boldsymbol{\sigma}, \quad (27)$$

where $\hat{\epsilon}$ is the light polarization unit vector and $\boldsymbol{\sigma}$ is the atomic polarization. Along with the change to α, there is an associated shift of the ground-state magnetic sublevels. The spin dependence of this energy shift $(\hat{k} \times \hat{\epsilon}) \cdot \boldsymbol{\sigma}$ is equivalent to a Zeeman shift from an effective magnetic field in the $\hat{k} \times \hat{\epsilon}$ direction. An EDM-like systematic can thus arise if the light polarization, applied electric field, and magnetic field are aligned such that $\hat{k} \times \hat{\epsilon}$ has a projection along the main magnetic field direction.

The absolute magnitude of $\delta\alpha$ for the $F = 1/2$ and $F = 3/2$ hyperfine components is the same, but the contributions have opposite sign. The absorptivity for the $F = 3/2$ component is twice that of the $F = 1/2$ component, and therefore $(\frac{\delta\alpha}{\alpha})_{3/2} = -\frac{1}{2}(\frac{\delta\alpha}{\alpha})_{1/2}$. The fractional change in the transition's absorptivity is equal to the fractional change in the optical pumping rate $\delta\Gamma_p/\Gamma_p$. The light shift and the light absorption

can be linked through the Karmers-Kronig relations; the energy shift for a ground-state sublevel is then

$$\delta\Omega_F = \frac{\Delta_F}{\gamma}\delta\Gamma_{p_F} = \frac{\Delta_F}{\gamma}\Gamma_{p_F}\left(\frac{\delta\alpha}{\alpha}\right)_F, \quad (28)$$

where Δ_F is the laser detuning from the transition center frequency, γ is the transition linewidth, and the subscript F refers to a particular hyperfine line.

For a detuning midway between the two hyperfine lines (as used for the Ref. [7] measurements), the summed contribution from the two lines is

$$\delta\Omega_{1/2} + \delta\Omega_{3/2} = \frac{\Delta_{1/2}}{\gamma}\left[\Gamma_{p_{1/2}}\left(\frac{\delta\alpha}{\alpha}\right)_{1/2} - \Gamma_{p_{3/2}}\left(\frac{\delta\alpha}{\alpha}\right)_{3/2}\right]. \quad (29)$$

Combining $\Gamma_{p_{3/2}} = 2\Gamma_{p_{1/2}}$ with $(\frac{\delta\alpha}{\alpha})_{3/2} = -\frac{1}{2}(\frac{\delta\alpha}{\alpha})_{1/2}$, Eq. (29) becomes

$$\delta\Omega_{1/2} + \delta\Omega_{3/2} = \frac{\Delta_{1/2}}{\gamma}\left[\frac{2}{3}\Gamma_p\left(\frac{\delta\alpha}{\alpha}\right)_{1/2}\right], \quad (30)$$

where Γ_p is the experimentally relevant total pumping rate. For the parallel electric and magnetic fields in Ref. [7], the angular dependence for Eq. (27) becomes $\sin\phi\cos\phi$, where ϕ is the angle between $\hat{\epsilon}$ and $\boldsymbol{E}$ and the quantization axis is taken along $\boldsymbol{E}$. The change in the ground-state Larmor frequency is then twice the energy shift of one of the $F = 1/2$ sublevels:

$$\delta\Omega_L = 2\cos\phi\sin\phi(\delta\Omega_{1/2} + \delta\Omega_{3/2}). \quad (31)$$

Preliminary measurements of $a_{M1} + a_{E2}$ were performed while acquiring the Ref. [7] data. These measurements used two separate orientations for the electric and main magnetic field: $|\hat{e} \cdot \hat{b}| = 1$ (the nominal EDM search configuration) and $|\hat{e} \cdot \hat{b}| = 0$, where $\hat{e}$ and $\hat{b}$ are unit vectors for the electric and magnetic field, respectively. For the former, $\hat{\epsilon}$ was alternated between $\pm 45°$ about $\hat{e}$ for Γ_p between $\sim 1/500$ s^{-1} and $1/150$ s^{-1}. For the latter, $\hat{\epsilon}$ was alternated between $0°$ and $90°$ about $\hat{e}$ for $\Gamma_p \sim 1/90$ s^{-1}. Together, these measurements gave

$$a_{M1} + a_{E2} = 3.9 \pm 3.2 \times 10^{-9} \text{ (kV/cm)}^{-1} \quad (32)$$

or a 1-σ upper limit of $(a_{M1} + a_{E2}) < 7.1 \times 10^{-9}$ (kV/cm)$^{-1}$. More recent studies [28], which use an independent data set collected after publication of the Ref. [7] results, give

$$a_{M1} + a_{E2} = 5.8 \pm 1.5 \times 10^{-9} \text{ (kV/cm)}^{-1} \quad (33)$$

or a 1-σ upper limit of $(a_{M1} + a_{E2}) < 7.3 \times 10^{-9}$ (kV/cm)$^{-1}$. Both values are in good agreement with the relativistic, many-body calculations described in Ref. [27], which predict $a_{M1} + a_{E2} = 8.0 \times 10^{-9}$ (kV/cm)$^{-1}$. Equation (32) places a 1-σ bound on the Stark interference systematic error of $0.19\sin\phi\cos\phi$ nHz or $21.3\sin\phi\cos\phi \times 10^{-30}$ e cm at $\Gamma_p = 1/200$ s^{-1}.

For vessel 2, $\Gamma_p \sim 1/400$ s^{-1} and $\phi \leqslant 2°$, which gives a systematic error of 0.36×10^{-30} e cm. For vessel 1, $\Gamma_p \sim 1/200$ s^{-1} and $\phi \leqslant 5°$, which gives a systematic error of 1.8×10^{-30} e cm. The data collected with the two vessels have roughly equal statistical weights; taking the mean, we arrive at a systematic error due to Stark interference of 1.09×10^{-30} e cm.

E. E^2 effects

A variety of systematic shifts are proportional to the square of the electric field. Some typical examples include frequency shifts due to absorptivity changes caused by the quadratic Stark effect, vector light shifts coupled to Kerr effect-induced changes to the light polarization, and motion of the vapor cells in background magnetic field gradients due to electrostatic forces or electrostriction. E^2 effects depend only on the magnitude of $\boldsymbol{E}$ and should cancel when taking the difference between frequencies measured at opposite HV polarities (e.g., the middle difference frequency $\nu_{MT} - \nu_{MB}$). If, however, the electric field does not reverse perfectly, then E^2 effects can lead to residual $|\boldsymbol{E}|$ shifts that mimic an EDM.

To set limits on this broad class of possible systematics, tests for frequency shifts correlated with $|\boldsymbol{E}|$ were performed by taking one or more runs per data sequence with a quadrupole HV pattern $(+0\text{-}0+0)$. The quadrupole runs were analyzed in the same manner as the dipole HV runs, except that the ± 10-kV scans were compared to the 0's. From this data, we find the shift in $\Delta\nu_{EDM}$ at ± 10 kV compared to zero field was less than 0.27 nHz.

The electric field reversibility in the EDM vapor cells was checked by repeated measurements of the scalar Stark shift of the $6\,^1S_0 \rightarrow 6\,^3P_1$ transition via a procedure similar to the one used in Ref. [13]. In each case, independent measurements were performed for the two middle vapor cells. These studies indicate an electric field reversibility of better than 2%. Combining this value with the upper limit obtained from the quadrupole runs gives a systematic error due to E^2 effects of 0.62×10^{-30} *e* cm.

F. Charging currents

Switching the HV polarity during the optical pumping phase generates charging currents that are up to four orders of magnitude larger than the steady-state leakage currents which occur during the probe phase. Charging currents can produce EDM-like signals if the resulting magnetic fields leave an imprint on the magnetic shields or, for example, magnetize trace ferrous metal contaminants. These currents were regularly altered during the course of the experiment by cycling (on adjacent runs) between HV ramp rates of 4, 2, 1, and 0.67 kV/s, leading to vessel (cell) currents ranging between ~ 3.5 and 13 nA (~ 1 to 3.8 nA). Figure 17 shows $\Delta\nu_{EDM}$ and $\Delta\nu_{Ave}$ versus the vessel charging current. $\Delta\nu_{Ave}$ is the change in the average precession frequency under HV reversal. Linear fits to the data give correlation slopes of (23.9 ± 33.4) pHz/nA and (-0.14 ± 1.58) nHz/nA, respectively. In both cases, the correlations are unresolved and each data set is consistent with a single mean ($\chi^2/\nu = 0.49$ and 1.4 for $\Delta\nu_{EDM}$ and $\Delta\nu_{Ave}$, respectively). Note that if the charging currents magnetized local sites (i.e., ferrous contaminants), then the cell, electrode, and vessel swaps performed at the sequence level should randomize the feedthrough (which could possibly appear as a correlation between $\Delta\nu_{EDM}$ and the cells, electrodes, or vessels). As shown in Ref. [7], however, the data set is apparently free of such problems.

A coherent feedthrough, however, could occur if the charging currents magnetized the magnetic shielding, a scenario that would lead to correlations between $\Delta\nu_{Ave}$ and the charging
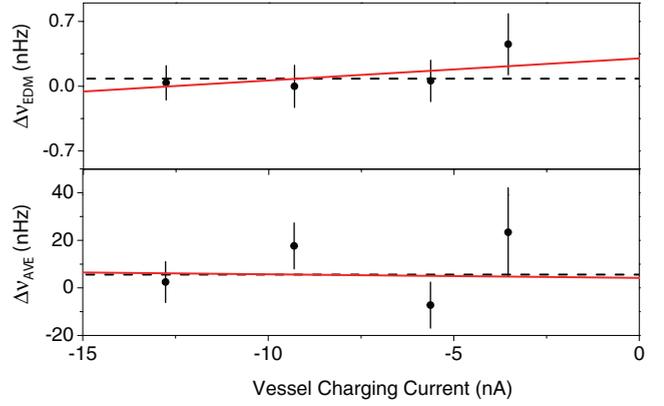

FIG. 17. (Color online) The top (bottom) panel shows $\Delta\nu_{EDM}$ ($\Delta\nu_{Ave}$ versus the vessel charging current. The solid (dashed) lines are least-squares linear fits (the error-weighted mean).

currents. From Fig. 17, the 1-σ limit for this unresolved correlation is 1.72 nHz/nA. Because $\Delta\nu_{EDM}$ is only sensitive to changes in the third derivative of the magnetic field, we take $\Delta\nu_{EDM} \approx \Delta\nu_{Ave}\, d^3/D^3 \leqslant 2 \times 10^{-4}\Delta\nu_{Ave}$, where d is the distance between the middle cells and D is the diameter of the inner shield. This estimate agrees with the reproducibility of the field gradients after shield degauss and with the change in the gradients when the main coil current is changed. Using this suppression factor and an average charging current of 10 nA, the systematic error due to charging currents is $(1.72 \text{ nHz/nA}) \times (10 \text{ nA}) \times (2 \times 10^{-4}) = 3.5$ pHz or 0.40×10^{-30} *e* cm.

G. Motional magnetic fields

An atom moving with velocity $\boldsymbol{v}$ through a region of nonzero electric field experiences a magnetic field in its rest frame that to first order in v/c (where c is the speed of light) is given by

$$\boldsymbol{B}_{\text{mot}} = \frac{\boldsymbol{v}}{c} \times \boldsymbol{E}. \tag{34}$$

In our experiment B_{mot} is much smaller than B, the magnetic field in the laboratory frame. If the angle θ_{EB} between the electric field and the laboratory magnetic field is small, the magnitude of the effective magnetic field experienced by the atom is, to second order in B_{mot},

$$B_{\text{eff}} = B + \theta B_{\text{mot}} + \frac{1}{2}\frac{B_{\text{mot}}^2}{B}, \tag{35}$$

where $|\theta| \leqslant \theta_{EB}$ and θB_{mot} is the projection of B_{mot} along B. B_{mot} can lead to an EDM-like systematic shift under two conditions: First, if $\theta_{EB} \neq 0$, the precession frequency can shift linearly with the electric field strength, and second, if $\theta_{EB} = 0$, B_{mot} can produce a false EDM if the electric field does not reverse perfectly when the HV polarity is flipped.

In vapor-cell experiments, motional field effects are suppressed in first order by the vanishing of the average atom velocity, $\langle \boldsymbol{v} \rangle = 0$. Finite $\boldsymbol{v}/c \times \boldsymbol{E}$ shifts, however, can still arise if the average velocity for the *polarized* atoms is nonzero. Such asymmetries can occur, for example, if the spins preferentially relax at a single point on the vapor-cell wall or if, on average,

the atoms are polarized near the front of the cell but analyzed near the middle of the cell.

To place limits on these possibilities, consider a spin-$\frac{1}{2}$ particle moving along the light-beam direction, taken as the x axis, in the presence of a magnetic field along $\hat{z}$ and a transverse electric field E_y along $\hat{y}$. The magnetic field causes the spin to precess in the x-y plane; E_y produces a motional magnetic field that adds linearly to B_z. The net phase angle through which the spin precesses is

$$\phi(x,t) = \gamma B_z t + \frac{\gamma}{c} \int_0^t v_x E_y \, dt'$$
$$= \gamma B_z t + \frac{\gamma}{c}[x(t) - x_0] E_y, \qquad (36)$$

where $x(t)$ (x_0) is the particle position at time t (time $t = 0$) and γ is the gyromagnetic ratio. The motional-field induced phase [i.e., the second term in Eq. (36)] thus depends only on the particle position. In the current experiment, wherein the spin orientation is detected by the induced rotation of the plane of polarization of a nonresonant probe beam, every atom along the beam path contributes equally to the total rotation signal. The rotation signal is then set by the average phase angle along the beam, $\langle \phi(t) \rangle$, where

$$\langle \phi(t) \rangle = \gamma B_z t + \frac{\gamma}{c} E_y (\langle x(t) \rangle - \langle x_0 \rangle). \qquad (37)$$

The $\boldsymbol{B}_{\text{mot}} = \boldsymbol{v}/c \times \boldsymbol{E}$ motional frequency shift is then

$$\Delta \omega_{\text{mot}} = \frac{\gamma E \sin\theta_{\text{EB}}}{c} \frac{d}{dt} \langle x(t) \rangle, \qquad (38)$$

where

$$\langle x(t) \rangle = \frac{\int_0^{2a} P(x,t) \, x \, dx}{\int_0^{2a} P(x,t) \, dx}, \qquad (39)$$

with a the cell radius and $P(x,t)$ the spin distribution along the beam path. For spatially uniform spin decay [i.e., $P(x,t) = P(x,0) e^{-\Gamma t}$], the $\boldsymbol{v} \times \boldsymbol{E}$ phase is time-independent, so the systematic error $\Delta \omega_{\text{mot}} = 0$. Generating $\Delta \omega_{\text{mot}} \neq 0$ then requires $\langle x(t) \rangle$ to evolve in time via asymmetric diffusion.

For EDM data, we pump the atoms on resonance where the vapor absorptivity is high and probe the spin precession off resonance, resulting in a potential translation of $\langle x(t) \rangle$ during the probe phase. We estimate the magnitude of this translation by considering the one-dimensional diffusion equation: $\partial P / \partial t = D(\partial^2 P / \partial x^2)$, where the diffusion constant $D \simeq 0.3$ cm^2 s^{-1} at the experimentally relevant buffer gas pressure. The general solution is

$$P(x,t) = \sum_n [u_n \cos(\alpha_n x) + v_n \sin(\alpha_n x)] e^{-\Gamma_n t}, \qquad (40)$$

where n is the diffusion mode index and $\Gamma_n = D\alpha_n^2$. Using $a = 1.25$ cm and a total spin relaxation rate $\Gamma = 1/200$ s, we find $\Gamma_0 \sim \Gamma$ and $\Gamma_1 \sim 1/2.1$ s for the simple case in which all spin relaxation takes place at the $x = 2a$ end. Thus, after a few seconds, as a result of the relatively fast diffusion ($D/a^2 \gg \Gamma$), the spin distribution settles into the slowly decaying $n = 0$ mode; in this equilibrium distribution the centroid $\langle x_{\text{eq}} \rangle$ is displaced from cell center by only $+0.01$ cm despite highly asymmetric relaxation.

Using the pump-phase cell absorptivity of 3.5 and final polarization of $\sim 75\%$, the light intensity profile at the end of the pump phase can be modeled as $I(x) \approx e^{-0.875x/2a}$. If we ignore diffusion during the pump phase, we can conservatively assume that the spin distribution has the same spatial dependence as the light intensity, leading to a spin density centroid displaced from cell center by -0.18 cm. Taking $t = 0$ at the end of the pump phase, it follows that $\langle x(t) \rangle - \langle x_{\text{eq}} \rangle \approx -0.19 e^{-\Gamma_1 t}$ cm, where $1/\Gamma_1 = 2.1$ s as above. Because we wait at least 6 s before analyzing probe-phase signals, most of the translation has taken place, and the total remaining translation of the beam centroid during the analyzed probe phase is less than 0.011 cm. From Eq. (38), with $\theta_{\text{EB}} \leqslant 0.02$ rad, it follows that $\Delta d_{\text{mot}} \leqslant 1.5 \times 10^{-31}$ e cm.

The average diffusion mode velocity is so small that it is useful to consider other possible sources for $d\langle x \rangle / dt$ such as slow changes to the beam pointing caused, for example, by hysteresis in the doubling cavity piezoelectric transducers. From measurements performed with a quadrant detector in one of the outer beam paths, we find that HV correlated motions of the probe beam are $\leqslant 40$ nm, leading to $\Delta d_{\text{mot}} \leqslant 5.4 \times 10^{-35}$ e cm for $\theta_{\text{EB}} \leqslant 0.02$ rad.

H. Convection

The energy deposited into the Hg vapor by the UV pump and probe beams can potentially create convection within the vapor cells that, in the presence of electric field gradients, may lead to additional motional magnetic field effects. To estimate the size of this systematic error, we need to determine the characteristic convective velocities.

We start by considering the thermal time constants within the vapor as given by the heat equation:

$$\frac{\partial T}{\partial t} = \alpha \nabla^2 T, \qquad (41)$$

where T is the departure of the cell temperature from equilibrium and $\alpha \approx 2 \times 10^{-5}$ m^2/s is the thermal diffusivity of the CO vapor. Boundary conditions of constant temperature at the cell walls provide a basis set for the thermal modes:

$$T(\rho,\phi,z) = \sum_{l,m,n} A_{lmn} e^{im\phi} \sin(l\pi z/L) J_0(x_{0n}\rho/a), \qquad (42)$$

where $L = 1.1$ cm is the vapor-cell height, $a = 1.25$ cm is its radius, and x_{0n} is the nth zero of the Bessel function J_0. The lowest-order mode has a relaxation time constant of $\tau_{101}^{-1} = \alpha[(\pi/L)^2 + (x_{01}/a)^2] = 0.4$ s^{-1}. Because τ is much shorter than the time we wait between the pump phase and analyzed probe phase ($\geqslant 6$ s), we need only consider convection produced by the UV light heating during the probe phase.

During the probe phase, roughly $P = 0.3$ μW of heat is deposited into the vapor cell within the 2×2-mm cross-sectional area of the probe beam. We estimate the steady-state temperature rise at the edges of the probe beam by solving the Poisson equation:

$$\nabla^2 T = -\frac{\dot{q}}{\kappa}, \qquad (43)$$

where $\dot{q}$ is the rate at which heat is deposited per unit volume and $\kappa \approx 2.5 \times 10^{-2}$ W/(K-m) is the thermal conductivity of the CO vapor. Using the Green's function for a point charge within a grounded cylindrical box [29], we integrate a line of point charges along the probe beam path within the cell to find the potential (temperature rise) at the outer edges of the probe beam. We find a maximum temperature rise of $\Delta T \leqslant 0.4$ mK, occurring near the center of the cell.

With a temperature differential of 0.4 mK, a characteristic length of 1 cm, and a kinematic viscosity $\nu = 1.6 \times 10^{-5}$ m^2/s for CO gas, we find a Grashof number, the ratio of buoyant forces to viscous forces, of Gr ≈ 0.04 and a Rayleigh number, the ratio of convective heat transfer to conductive heat transfer, of Ra ≈ 0.03 for fluid flow within the vapor cells. Nonetheless, buoyant forces will drive flow at some level. To estimate the flow velocities, we turn to low Grashof number analytic studies of convection between concentric horizontal cylinders maintained at different temperatures [30]. Even at low Grashof number, a "creeping-flow" convection solution was found with the characteristic kidney shape flow profile on either side of the inner horizontal cylinder. If we approximate our vapor cell as a horizontal cylinder of radius $b = 0.93$ cm ($\pi b^2 = 2aL$), with a central cylindrical heat source of radius 1 mm, then we can use the results of Ref. [30] and find a maximum flow speed of $\leqslant 2 \times 10^{-5}$ cm/s.

The symmetry of the creeping-flow convection lobes on either side of the pump beam would require an unphysical configuration of electric field gradients to produce a significant motional magnetic field systematic error. Nonetheless, as a worst-case scenario we take Eq. (38) with $\theta_{\rm EB} \leqslant 0.1$ rad and $d\langle x(t) \rangle/dt = 2 \times 10^{-5}$ cm/s to set an upper limit on the convection systematic error of $\Delta d_{\rm conv} \leqslant 2.2 \times 10^{-31}$ e cm.

I. Geometric or Berry's phase effects

Geometric phase effects, first identified by Ref. [31] in the context of atomic beam experiments, arise due to the inevitable presence of magnetic field gradients. In this case, the motional magnetic field interacts with transverse gradient components of the applied magnetic field, leading to HV correlated shifts of the Larmor precession frequency. Specifically, if the main magnetic field $\boldsymbol{B}_0 = B_0 \hat{y}$ has a nonzero gradient $\partial B_0/\partial y \neq 0$, then $\nabla \cdot \boldsymbol{B} = 0$ implies that $\boldsymbol{B}_0$ will also have a nonzero radial component $B_r = (r/2)\partial B_0/\partial y$. As a particle or atom moves through the storage cell, it will experience a transverse motional magnetic field ($\boldsymbol{B}_0$ and the applied electric field $\boldsymbol{E}$ are assumed to be parallel). The motional field adds to B_r, causing the magnitude of the total magnetic field to depend linearly on the electric field. This effect has been treated analytically in Ref. [32] by considering the velocity autocorrelation function of the moving particles.

Following this treatment, the geometric phase frequency shift is given by

$$\delta \nu_G = \frac{abR^2}{2\pi} \frac{4}{x_1^2 (x_1^2 - 1)} \frac{1}{\left(\omega_0 R^2/Dx_1^2\right)^2 + 1}, \quad (44)$$

where

$$a = \frac{\gamma}{2} \frac{\partial B_y}{\partial y} \quad \text{and} \quad b = \gamma \frac{E}{c}, \quad (45)$$

TABLE IV. Limits on *CP*-violating parameters (defined in the text) based on our new experimental limit for $d(^{199}$Hg) (95% C.L.) compared to limits from the YbF (90% C.L.) [38], Tl (90% C.L.) [37], neutron (90% C.L.) [47], or TlF (95% C.L.) [59] experiments. Values that improve upon (complement) previous limits appear above (below) the horizontal line. Particle theory interpretation references are given in the last column.

Parameter	^{199}Hg bound	Hg theory	Best other limit		
$\tilde{d}_q$(cm)[a]	6×10^{-27}	[58]	n:	3×10^{-26}	[60]
d_p(e cm)	8.6×10^{-25}	[46]	TlF	6×10^{-23}	[61]
C_{SP}	6.6×10^{-8}	[34]	Tl	2.4×10^{-7}	[62]
C_{PS}	5.2×10^{-7}	[39]	TlF	3×10^{-4}	[5]
C_T	1.9×10^{-9}	[39]	TlF	4.5×10^{-7}	[5]
$\bar{\theta}_{QCD}$	5.3×10^{-10}	[56]	n	2.4×10^{-10}	[60]
d_n(e cm)	6.3×10^{-26}	[46]	n	2.9×10^{-26}	[60]
d_e(e cm)	3×10^{-27}	[33,36]	YbF	1.05×10^{-27}	[60]

[a]For ^{199}Hg, $\tilde{d}_q = (\tilde{d}_u - \tilde{d}_d)$; for n, $\tilde{d}_q = (0.5\tilde{d}_u + \tilde{d}_d)$.

where γ is the gyromagnetic ratio, R is the cell radius, $x_1 = 1.84$, and $D = 0.3$ cm/s is the diffusion constant.

Taking $dB_y/dy \sim \delta\omega_y/\omega_y \sim 2 \times 10^{-6}$ (as shown in Fig. 7) and the known cell dimensions, Eq. (45) gives a Berry's phase systematic error of 0.18×10^{-31} e cm.

VIII. ^{199}Hg EDM RESULT

Using the statistical error from Sec. VI and the quadrature sum of the systematic errors shown in Table II leads to our final result:

$$d(^{199}\text{Hg}) = (0.49 \pm 1.29_{\rm stat} \pm 0.76_{\rm syst}) \times 10^{-29} e \text{ cm},$$

which we interpret as an upper limit of $d(^{199}$Hg$) < 3.1 \times 10^{-29}$ e cm (95% C.L.).

IX. INTERPRETATION OF RESULTS

In this section we discuss the implications of the ^{199}Hg EDM limit for possible new sources of *CP* violation. We derive the ^{199}Hg bounds on various *CP*-violating parameters, and compare with bounds from other EDM experiments. A summary of these limits is presented in Table IV. We also relate some of these limits to *CP* violation in supersymmetry and in Fig. 18 illustrate one way the ^{199}Hg EDM plays a key role in probing *CP* violation in supersymmetry.

We order the discussion by the four mechanisms that can generate an atomic EDM. These mechanisms are (i) an EDM of a valence electron, (ii) a P,T-violating electron-nucleon interaction, (iii) an EDM of a valence nucleon, or (iv) a P,T-violating nucleon-nucleon interaction. Various EDM experiments test these mechanisms to a greater or lesser degree. For instance, experiments on paramagnetic atoms are most sensitive to (i), whereas the neutron EDM search tests mainly (iii). We discuss the ^{199}Hg EDM sensitivity to all these mechanisms in the following sections and see that one of the most important is the last one, P,T-odd nuclear interactions. Any parameter bounds quoted refer to the limit on the ^{199}Hg EDM set by the experiment described in Ref. [7] and this paper.
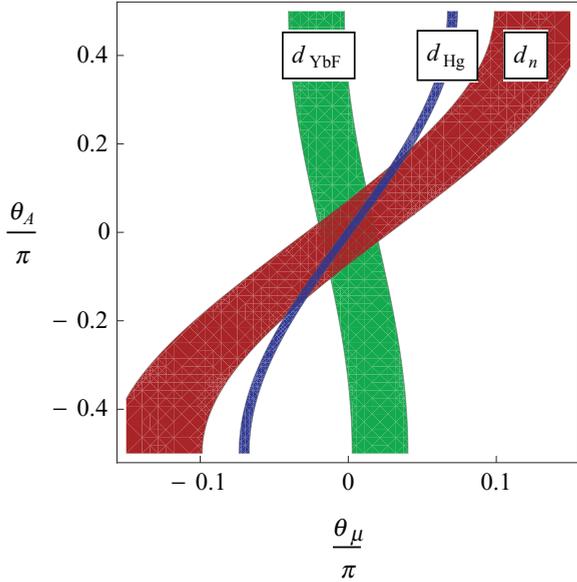
FIG. 18. (Color online) Limits set on *CP* violation in a simplified supersymmetric model (MSSM) by the combination of the three most sensitive EDM constraints (the neutron d_n, mercury d_{Hg}, and the electron EDM from d_{YbF}). The two *CP*-violating MSSM phase parameters are plotted for a generic mass scale of $M_{SUSY} = 1$ TeV and $\tan \beta = 3$. The allowed region is the overlap of the three bands. (Figure courtesy of Adam Ritz, updated from Ref [60].)

In establishing bounds on possible new sources of *CP* violation, we make the assumption that only the source under consideration contributes to d_{Hg}.

A. Leptonic mechanisms

1. Electron EDM

Despite the fact that mercury is diamagnetic, the limit on the EDM of ^{199}Hg can still be used to set a bound on the electron EDM d_e. An electron EDM can generate an EDM of the mercury atom through the hyperfine interaction. The dominant contribution arises at third order in perturbation theory [5]. There is another contribution at second order [33,34], arising from the interaction of the electron EDM with the magnetic field of the nucleus.

Extrapolating from a calculation of the ^{199}Hg atomic EDM induced by the *P*,*T*-violating tensor-pseudotensor electron-nucleon interaction C^T [35], the authors of [33] estimated an electron EDM "enhancement" factor for ^{199}Hg,

$$d_{Hg} = -0.014 d_e. \tag{46}$$

A time-dependent Hartree-Fock calculation of the same effects [36] found a substantially different result,

$$d_{Hg} = 0.0116 d_e. \tag{47}$$

The discrepancy is due to large polarization corrections from the lowest-order calculation, and further corrections from correlation effects might alter this result. However, both factors are of the same magnitude, and either may be used along with the result of [7] to derive a limit on the electron EDM of

$$|d_e| < 3 \times 10^{-27} \ e \ \text{cm}. \tag{48}$$

This limit is within a factor of two of the limit derived from the Tl beam experiment [37] and within a factor of three of the limit derived from the recent YbF beam experiment [38]. Improved theoretical calculations may allow a more strict bound on d_e to be derived from the bound on d_{Hg}.

2. Electron-nucleon interactions

P,*T*-odd electron-nucleon interactions can be treated phenomenologically, and if the set of operators is restricted to four-fermion operators without derivatives, the interaction can be written

$$H = \frac{G_F}{\sqrt{2}} \sum_n \left(C_n^{SP} \bar{N} N \bar{e} i \gamma_5 e + C_n^{PS} \bar{N} i \gamma_5 N \bar{e} e \right.$$
$$\left. + C_n^T \bar{N} i \gamma_5 \sigma_{\mu\nu} N \bar{e} \sigma_{\mu\nu} e \right), \tag{49}$$

where the sum is over all the nucleons, G_F is the weak interaction coupling constant, N and e are nucleon and electron operators, respectively, γ_5 and $\sigma_{\mu\nu}$ are Dirac matrices, and C^S, C^P, and C^T are dimensionless constants that determine the strength of the scalar-pseudoscalar, pseudoscalar-scalar, and tensor interactions, respectively [5,34,39]. In the limit of infinite nuclear mass, the pseudoscalar-scalar term vanishes, and so this term is less effective at generating atomic EDMs. Of the remaining terms, the scalar-pseudoscalar term depends on the electronic angular momentum and so does not directly contribute to the EDM of ^{199}Hg. However, when combined with the hyperfine interaction, it can induce a diamagnetic EDM at third order in perturbation theory. The tensor term contributes directly to the ^{199}Hg atomic EDM; its influence has been calculated in Ref. [39], and making use of the limit on the ^{199}Hg EDM, a bound of

$$C_T \leqslant 1.9 \times 10^{-9} \tag{50}$$

was obtained. Another recent calculation [40] employing relativistic coupled-cluster methods obtained a somewhat more stringent upper bound on the tensor interaction coefficient, $C_T \leqslant 1.4 \times 10^{-9}$. The limit on the mercury EDM sets the best limit on C_T. The pseudoscalar-scalar coefficients can be related to C_T [33,34,39], resulting in

$$C_{PS} \leqslant 5.2 \times 10^{-7}. \tag{51}$$

The scalar-pseudoscalar interaction can generate an EDM of a diamagnetic atom at third-order in perturbation theory, along with the hyperfine interaction. It can also be related to the tensor interaction [33,34], and so along with (50) a limit of

$$C_{SP} \leqslant 6.6 \times 10^{-8} \tag{52}$$

can be obtained.

B. Hadronic mechanisms

An EDM of ^{199}Hg can be produced by an EDM of an unpaired nucleon or by *CP*-violating forces between nucleons in the nucleus. The limits placed on *CP* violation in this hadronic sector can be more sensitive to new physics but also more uncertain than those from the lepton sector. In addition to atomic theory, difficult nuclear structure and QCD calculations are required to relate the atomic EDM to more fundamental

objects such as the EDMs and chromo-EDMs (CEDMs) of the quarks within the ^{199}Hg nucleus.

1. Schiff moment

In the limit of purely electrostatic forces, when an atom is subjected to an external electric field, its electron cloud distorts, screening the field so that the nuclear charge feels no net electric force (otherwise, the nucleus would be accelerated by a uniform external field). Thus, with a pointlike nucleus the external field cannot interact with a nuclear EDM, and there will be no energy shift [41]. In real atoms this screening is incomplete, due mainly to the finite size of the nucleus in the case of heavy atoms. The nuclear charge and EDM distributions are different in general, allowing the average nuclear EDM effect to be finite. The size of this effect is given by the Schiff moment S, the lowest-order unscreened P,T-violating nuclear moment, and thus the atomic EDM due to hadronic mechanisms is commonly parametrized in terms of S.

Several calculations [39,40,42,43] of the ^{199}Hg atomic EDM induced by its nuclear Schiff moment have been made. The most recent [39] was a calculation employing the configuration interaction technique to assess the contribution of valance electrons, and many-body perturbation theory with random-phase approximation methods to deal with the electron core, which found

$$d(^{199}\text{Hg}) = -2.6 \times 10^{-17} \left(\frac{S}{e \, \text{fm}^3} \right) e \, \text{cm}. \quad (53)$$

We note that another recent calculation employing relativistic coupled-cluster methods found a somewhat increased ($\sim 2\times$) sensitivity of the ^{199}Hg atomic EDM to the nuclear Schiff moment [40]. The value for the S obtained in Ref. [39] is about 30% smaller than the value from an older calculation [42]. This older value was an estimate obtained from a calculation of the ^{199}Hg EDM induced by the P,T-violating electron-nucleon tensor interaction [35]. We also point out that there remains some controversy as to whether the usual expression for the Schiff moment is correct [44,45].

Using the bound on the ^{199}Hg atomic EDM [7] and Eq. (53), we can derive an upper limit on the ^{199}Hg Schiff moment of

$$|S(^{199}\text{Hg})| \leqslant 1.2 \times 10^{-12} \, e \, \text{fm}^3. \quad (54)$$

2. Nucleon EDMs

The Schiff moment of the ^{199}Hg nucleus can be induced by the EDMs of its constituent nucleons. In the simple shell model of the ^{199}Hg nucleus, the nuclear spin $I = 1/2$ is entirely due to a single valence neutron. The Schiff moment is then due mainly to the EDM of this valence neutron, though EDMs of protons in the nuclear core also contribute due to configuration mixing. Under these simple assumptions, the ^{199}Hg Schiff moment has been estimated to be [43]

$$S = (2.2d_n + 0.2d_p) \, \text{fm}^2. \quad (55)$$

A more sophisticated calculation performed recently accounted for the polarization of core protons by the P,T-violating dipole field of the valence neutron [46]. The result

of this calculation was

$$S = (1.9d_n + 0.2d_p) \, \text{fm}^2. \quad (56)$$

This result, in combination with the relationship (53) between the atomic dipole moment and S, can be used to place limits on the EDMs of the nucleons. From the limit on the Schiff moment of ^{199}Hg and Eq. (56), we have the following bounds on the nucleon EDMs:

$$d_n \leqslant 6.3 \times 10^{-26} \, e \, \text{cm}, \quad (57)$$

$$d_p \leqslant 8.6 \times 10^{-25} e \, \text{cm}, \quad (58)$$

where the limit on the proton EDM has been relaxed to account for the 30% theoretical uncertainty claimed in Ref. [46]. The bound on the neutron EDM from the ^{199}Hg experiment is only about a factor of two worse than the direct bound on the neutron EDM [47], and the the limit (58) is the best constraint on d_p.

3. P,T-violating nucleon-nucleon interactions

The dominant contribution to the ^{199}Hg EDM is expected to be from P,T-violating nucleon-nucleon interactions, because of the small pion mass and the strong P,T-conserving πNN coupling constant $g = 13.5$. The contribution to the Schiff moment from these interactions is expected to be one to two orders of magnitude larger than that generated directly by the nucleon EDMs [42,48].

The P,T-odd nucleon-nucleon interaction can be modeled as a finite-range interaction [49],

$$\begin{aligned} W(\boldsymbol{r}_1 - \boldsymbol{r}_2) = &-\frac{g}{8\pi m_N} \boldsymbol{\nabla}_1 \frac{e^{-m_\pi r_{12}}}{r_{12}} \\ &\times \{[(\bar{g}_0 \boldsymbol{\tau}_1 \cdot \boldsymbol{\tau}_2 + \bar{g}_2(\boldsymbol{\tau}_1 \cdot \boldsymbol{\tau}_2 - 3\tau_{1z}\tau_{2z})] \\ &\times (\boldsymbol{\sigma}_1 - \boldsymbol{\sigma}_2) + \bar{g}_1(\tau_{1z}\boldsymbol{\sigma}_1 - \tau_{2z}\boldsymbol{\sigma}_2)\}, \quad (59) \end{aligned}$$

where m_π is the pion mass, m_N is the nucleon mass, the $\boldsymbol{\sigma}_{1,2}$ are the nucleon spins, the $\boldsymbol{\tau_{1,2}}$ are vectorized Pauli spin matrices, r_{12} is the interparticle separation, and the constants $\bar{g}_0$, $\bar{g}_1$, and $\bar{g}_2$ determine the strengths of the isoscalar, isovector, and isotensor couplings, respectively.

A calculation employing this finite range interaction found that the ^{199}Hg Schiff moment is given in terms of the pion-nucleon coupling constant by [49,50]

$$\begin{aligned} S(^{199}\text{Hg}) \\ = (-0.000\,04g\bar{g}_0 - 0.055g\bar{g}_1 + 0.009g\bar{g}_2) \, e \, \text{fm}^3. \quad (60) \end{aligned}$$

This calculation employed the random-phase approximation (RPA) and took into account the polarization of the nuclear core by the field of the valence neutron. We see that the isoscalar and isotensor couplings are significantly suppressed. This suppression results from the cancellation of the single-particle effects by the collective core-polarization effects, and thus it is possible that inaccuracies in the many-body calculations could lead to a substantial modification of the coefficients of g_0 and g_2 in Eq. (60). The authors have performed similar calculations for other nuclei [50], and in none of these other calculations is this cancellation so precise.

Another calculation attempts to address some of these issues by performing a similar many-body calculation of the ^{199}Hg Schiff moment using a variety of phenomenological models for the strong interactions [51]. These authors find that

the ^{199}Hg Schiff moment is given by

$$S(^{199}\text{Hg})$$
$$= (0.010g\bar{g}_0 + 0.074g\bar{g}_1 + 0.018g\bar{g}_2)\, e\,\text{fm}^3. \qquad (61)$$

The reduction of the isoscalar and isotensor couplings from the first-order result (62) is not as severe as that found by [49,50]. The authors note that their use of several phenomenological interactions enables them to have some idea of the uncertainty in their calculations. Their values for the isoscalar, isovector, and isotensor coupling constants vary over a range of 5, 1.6, and 2.3, respectively.

The most recent calculation of the ^{199}Hg Schiff moment in terms of nuclear parameters is in conflict with both of the calculations described above [52]. These authors performed a fully self-consitent mean field calculation of the Schiff moment, taking into account core polarization effects and allowing for deformation of the ^{199}Hg nucleus. As in Ref. [51], several phenomenological nuclear potential models were employed. The isoscalar and isotensor coefficient values found tended to be larger than in Refs. [50,51], but the important isovector coefficient was found to be significantly suppressed.

It is interesting to note that a much earlier calculation Refs. [42,48] used a nucleon-nucleon contact interaction in the nuclear shell model, and obtained a result that can be interpreted [49] in terms of the current notation as

$$S(^{199}\text{Hg}) \sim -0.09g(\bar{g}_0 + \bar{g}_1 - 2\bar{g}_2)\, e\,\text{fm}^3. \qquad (62)$$

We see that the older calculation misses the isoscalar and isotensor suppression, as expected, but gives an isovector coupling reasonably consistent with the modern values.

In this paper we opt to use the coefficient values from [51], in order to be consistent with our earlier letter [7]. However, it must be noted that although the nuclear physics calculations involved in the interpretation of the ^{199}Hg EDM limit are complicated and further work in this area may result in significant revision of the results presented above, it is possible that the isovector coupling is suppressed as predicted by [52] and that the sensitivity of the ^{199}Hg EDM to fundamental physics is therefore somewhat reduced.

C. Generators of *CP*-violating nuclear interactions

There are several sources that could generate the *CP*-violating pion-nucleon coupling discussed above. The most important of these are the effective θ term in the QCD Lagrangian and the chromoelectric dipole moments (CEDMs) of the quarks.

1. Strong CP violation: $\bar{\theta}$

The most general form of the QCD Lagrangian includes a *CP*-violating term [53],

$$L_\theta = \frac{\theta}{2}\left(\frac{g}{4\pi}\right)^2 G_a^{\mu\nu} G_{a\mu\nu}^*, \qquad (63)$$

where $g/(4\pi)$ is the color coupling constant, a is the color index, and G, G^* are the gluonic field tensor and its complex conjugate. Weak interaction effects shift θ from its bare value

to the observable value,

$$\bar{\theta} = \theta + \arg[\det(M)], \qquad (64)$$

where M is the Kobayashi-Maskawa quark-mixing matrix.

The QCD θ term is an isoscalar, and it will contribute to the *CP*-violating isoscalar pion-nucleon coupling $\bar{g}_0$. The calculated $\bar{\theta}$ contribution to $\bar{g}_0$ is [54,55]

$$\bar{g}_0 = 0.027\bar{\theta}. \qquad (65)$$

It is difficult to trust a limit on $\bar{\theta}$ from the ^{199}Hg Schiff moment, due to the large theoretical uncertainty in the dependence of the Schiff moment on $\bar{g}_0$, as shown in Eqs. (62), (60), and (61). In any event the reduction of the isoscalar effects due to many-body shielding causes a reduction in sensitivity of the Schiff moment to $\bar{\theta}$. There is no equivalent reduction for the neutron, and thus the most reliable bound on $\bar{\theta}$ from ^{199}Hg is by means of the dependence of the EDM on the neutron EDM via Eq. (57).

A QCD sum-rule calculation of the neutron EDM in terms of $\bar{\theta}$ has also been performed [56], with the result

$$d_n = 1.2 \times 10^{-16}\bar{\theta}\, e\,\text{cm}. \qquad (66)$$

This, along with the current upper bound on the neutron EDM [47], is usually taken to be the most reliable limit on strong *CP* violation, yielding

$$\bar{\theta} \leqslant 2.4 \times 10^{-10}. \qquad (67)$$

Using Eq. (57) the limit from ^{199}Hg is about twice this value.

2. QCD calculation of EDMs

A *CP*-violating nucleon-nucleon interaction could also be generated by the chromoelectric dipole moments of the quarks. The underlying processes that generate these CEDMs are analogous to those that would generate a quark EDM, except that external photon interactions are replaced with gluon lines. Quark EDMs, while the dominant contribution to the neutron EDM (assuming that the $\bar{\theta}$ term is removed by the Peccei-Quin mechanism [57]), cannot produce a *CP*-odd pion-nucleon coupling and thus do not generate a Schiff moment except through their contribution to d_n.

The isovector *CP*-odd pion-nucleon coupling constant has been calculated using a QCD sum-rules technique [58]. The result,

$$\bar{g}_1 = 2^{+4}_{-1}(\tilde{d}_u - \tilde{d}_d) \times 10^{14}\,\text{cm}, \qquad (68)$$

where $\tilde{d}_u$ and $\tilde{d}_d$ refer to the CEDMs of the up and down quarks, can be used along with Eqs. (53) and (61) to set a bound,

$$|\tilde{d}_u - \tilde{d}_d| \leqslant 6 \times 10^{-27}\,\text{cm}. \qquad (69)$$

This bound would be slightly more or less restrictive if Eq. (62) or (60) had been used instead of (61). The sensitivity of the ^{199}Hg EDM experiment to new physics derives mainly from the bound it can place on this particular combination of quark CEDMs.

3. EDMs in supersymmetric models

The large number of new fields in supersymmetric models introduces many new *CP*-violating phases as well. Several

simplifying assumptions are commonly made to make discussion of *CP* violation in the minimally supersymmetric standard model (MSSM) less unwieldy, which along with suitable phase redefinitions reduce the number of independent phases to two, θ_A and θ_μ. These parameters introduce a complex phase at all quark-squark-gluino and fermion-sfermion-chargino or -neutralino vertices and can lead to quark EDM or CEDM production at the one-loop level within a single quark generation.

The bounds placed on the SUSY phases by the null results of the various EDM searches can only be interpreted within the context of a given set of model parameters. However, to demonstrate the reach of EDM experiments it is useful to consider a simplified model where all soft symmetry-breaking parameters including the superpartner masses are determined by a single mass scale M_{SUSY} and a dimensionless parameter $\tan \beta = \langle H_2 \rangle / \langle H_1 \rangle$, where $\langle H_{1,2} \rangle$ are the vacuum expectation values of the Higgs superfields. Then, for given values of M_{SUSY} and $\tan \beta$, the limits placed on the two phase parameters by the various EDM experiments can be plotted as in Fig. 18, in which the ^{199}Hg result plays a key role. One striking feature of such a plot is the complementarity of the different EDM bounds. For example, the electron EDM result (which is free of hadronic theory uncertainties) places tight constraints on the value of θ_μ, but cancellations among the various *CP*-violating SUSY processes that contribute make it relatively insensitive to θ_A. However, tight constraints are placed on θ_A by the neutron and especially the ^{199}Hg EDM results, and only a tiny region of the parameter space remains viable [60,63].

The analysis underlying Fig. 18 has been extended by a more comprehensive study of the limits EDM results can set on the MSSM parameter space [64]. These authors employ the second-order renormalization group equations and examine several "benchmark" scenarios, where the gaugino and sfermion masses and the $\tan \beta$ parameter vary over a wide range. In some of these scenarios tight bounds can be set on both phase parameters, but in others only one of the phases (θ_μ) is well constrained. When this analysis is updated with the new ^{199}Hg EDM results the bounds set by ^{199}Hg are usually comparable and complementary to those set by the electron and neutron EDM limits.

In most situations it is apparent that either the phase angles are unnaturally small, or the masses of the superpartners are significantly heavier than would otherwise have been predicted. Possible solutions to this so-called "SUSY *CP* problem" have been discussed [60,64].

X. CONCLUSION

Our recent upper bound on the permanent EDM of ^{199}Hg [7] is the most sensitive such bound on the EDM of a diamagnetic atom. This result sets new limits on *CP*-violating physics beyond the standard model. Because the mercury atom provides a rich hunting ground for sources of *CP* violation, we are in the process of upgrading the Hg EDM search experiment to improve its sensitivity.

As discussed in Sec. V, the experimental sensitivity of our recent EDM results does not approach the sensitivity allowed by shot noise estimates. We have identified several modifications to the existing EDM apparatus that should allow

a more sensitive search for an EDM of Hg to be undertaken. Magnetic field noise from thermally excited currents near to the vapor cells has been reduced by removing the conductors nearest to the cells. New EDM data runs will be taken by probing the Hg atom precession for 10 s, blocking the probe beam light for approximately 200 s, and then probing the precession for another 10–20 s. The difference between the precession phase of the final and initial probe periods provides a sensitive measure of the precession frequency of the atoms while they are in the dark while reducing noise and systematic errors due to the light. Wollaston polarizers have been mounted on each probe beam, doubling the number of detected photons used to measure Larmor precession. New leakage current monitors will measure separately the currents that flow through the dry gas surrounding the vapor cells and the currents that flow within and on the walls of the cells, providing better control of leakage current systematic errors. Finally, hydroxycatalysis bonding can be used in place of glue to construct new vapor cells in an attempt to better stabilize the long-term density of Hg vapor within the cells. With these upgrades in place, we anticipate a factor of five improvement in sensitivity to an EDM of Hg.

APPENDIX: MAGNETIC MATERIALS TESTING

Materials used in the construction of the cell vessel and electrodes were screened for ferromagnetic contaminants using a Quantum Designs MPMS-5S SQUID magnetometer system available in the University of Washington analytical chemistry laboratory. This instrument scans an applied field and analyzes the magnetization of the material under test, tracing out a susceptibility curve. Its specified resolution is 1×10^{-8} emu at an applied field of 2500 Oe. Ferrous metal contaminants were identified by the presence of a telltale hysteresis curve superimposed over a linear diamagnetic susceptibility.

Several suspect materials were identified. In particular, we found that a commercial silver paint that had been used to make electrical connections to the cells and electrodes contained
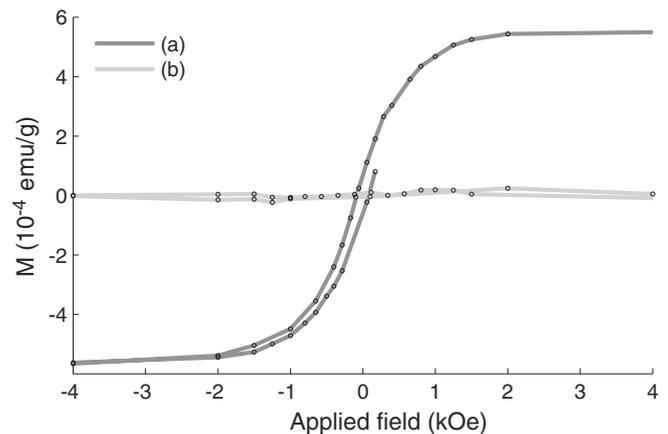

FIG. 19. Magnetization signal from gasket materials, with diamagnetic background removed. (a) Buna-N nitrile, formerly used for o-ring seals. (b) Dow-Corning Sylgard 184 silicone elastomer, which we pour into custom molds to make the gaskets and o-rings currently in use.

some ferromagnetic material, as did a silver-impregnated conductive rubber material, and Buna-N o-rings that were used to create gastight seals at the vessel windows and electrical feedthroughs (see Fig. 19). The commercial silver paint was replaced with a laboratory-made alternative, a clear acrylic varnish mixed with a fine 99.999% pure silver powder in a 1:1 weight ratio. The o-rings were replaced with laboratory-made gaskets, using a pourable silicone elastomer (Dow-Corning Sylgard 184). The new materials possess no measurable ferromagnetic signature.

[1] M. Kobayashi and T. Maskawa, Prog. Theor. Phys. **49**, 652 (1973).

[2] J. H. Christenson, J. W. Cronin, V. L. Fitch, and R. Turlay, Phys. Rev. Lett. **13**, 138 (1964).

[3] K. Abe *et al.*, Phys. Rev. Lett. **87**, 091802 (2001).

[4] A. D. Sakharov, Sov. Phys. Usp. **34**, 392 (1991).

[5] I. B. Khriplovich and S. K. Lamoreaux, *CP Violation Without Strangeness* (Springer, Berlin, 1997).

[6] B. L. Roberts and W. J. Marciano (eds.), *Advanced Series on Directions in High Energy Physics*, Vol. 20 (World Scientific, Singapore, 2009).

[7] W. C. Griffith, M. D. Swallows, T. H. Loftus, M. V. Romalis, B. R. Heckel, and E. N. Fortson, Phys. Rev. Lett. **102**, 101601 (2009).

[8] M. V. Romalis, W. C. Griffith, J. P. Jacobs, and E. N. Fortson, Phys. Rev. Lett. **86**, 2505 (2001).

[9] W. E. Bell and A. L. Bloom, Phys. Rev. Lett. **6**, 280 (1961).

[10] W. Happer, Rev. Mod. Phys. **44**, 169 (1972).

[11] W. Happer and B. S. Mathur, Phys. Rev. **163**, 12 (1967).

[12] C. Zimmerman, V. Vuletic, A. Hemmerich, and T. W. Hansch, Appl. Phys. Lett. **66**, 2318 (1995).

[13] D. M. Harber and M. V. Romalis, Phys. Rev. A **63**, 013402 (2000).

[14] T. W. Hansch and B. Couillaud, Opt. Commun. **35**, 441 (1980).

[15] M. D. Swallows, Ph.D. thesis, University of Washington, 2007.

[16] M. V. Romalis and L. Lin, J. Chem. Phys. **120**, 1511 (2004).

[17] C. Cioffi, R. Giannetti, V. Dattilo, and B. Neri, Proc. IEEE Trans. Instrum. Meas. **47**, 78 (1998).

[18] W. C. Griffith, Ph.D. thesis, University of Washington, 2005.

[19] W. B. Dress, P. D. Miler, J. M. Pendlebury, P. Perrin, and N. F. Ramsey, Phys. Rev. D **15**, 9 (1977).

[20] V. Shah, G. Vasilakis, and M. V. Romalis, Phys. Rev. Lett. **104**, 013601 (2010).

[21] Y. Chibane, S. K. Lamoreaux, J. M. Pendlebury, and K. F. Smith, Meas. Sci. Technol. **6**, 1671 (1995).

[22] T. Kornack, S. Smullin, S. Lee, and M. Romalis, Appl. Phys. Lett. **90**, 223501 (2007).

[23] S. Lee and M. Romalis, J. Appl. Phys. **103**, 084904 (2008).

[24] J. Hodgdon, B. R. Heckel, and E. N. Fortson, Phys. Rev. A **43**, 3343 (1991).

[25] X. Chen, F. R. Huang-Hellinger, B. R. Heckel, and E. N. Fortson, Phys. Rev. A **50**, 4729 (1994).

[26] S. K. Lamoreaux and E. N. Fortson, Phys. Rev. A **46**, 7053 (1992).

[27] K. Beloy, V. A. Dzuba, and A. Derevianko, Phys. Rev. A **79**, 042503 (2009).

[28] T. H. Loftus, M. D. Swallows, W. C. Griffith, M. V. Romalis, B. R. Heckel, and E. N. Fortson, Phys. Rev. Lett. **106**, 253002 (2011).

[29] J. D. Jackson, *Classical Electrodynamics* (Wiley & Sons, New York, 1975).

[30] S. Amano and H. Yoshinobu, Bull. Osaka Prefect. Univ., Ser. A **18**, 269 (1969).

[31] E. D. Commins, Am. J. Phys. **59**, 1077 (1991).

[32] S. K. Lamoreaux and R. Golub, Phys. Rev. A **71**, 032104 (2005).

[33] V. V. Flambaum and I. B. Khriplovich, Sov. Phys. JETP **62**, 872 (1985).

[34] J. S. M. Ginges and V. V. Flambaum, Phys. Rep. **397**, 63 (2004).

[35] A. M. Maartensson-Pendrill, Phys. Rev. Lett. **54**, 1153 (1985).

[36] A. Martensson-Pendrill and P. Oster, Phys. Scr. **36**, 444 (1987).

[37] B. C. Regan, E. D. Commins, C. J. Schmidt, and D. DeMille, Phys. Rev. Lett. **88**, 071805 (2002).

[38] J. J. Hudson, D. M. Kara, I. J. Smallman, B. E. Sauer, M. R. Tarbutt, and E. A. Hinds, Nature **473**, 493 (2011).

[39] V. A. Dzuba, V. V. Flambaum, and S. G. Porsev, Phys. Rev. A **80**, 032120 (2009).

[40] K. V. P. Latha, D. Angom, B. P. Das, and D. Mukherjee, Phys. Rev. Lett. **103**, 083001 (2009).

[41] L. I. Schiff, Phys. Rev. **132**, 2194 (1963).

[42] V. V. Flambaum, I. B. Khriplovich, and O. P. Sushkov, Nucl. Phys. A **449**, 750 (1986).

[43] V. A. Dzuba, V. V. Flambaum, J. S. M. Ginges, and M. G. Kozlov, Phys. Rev. A **66**, 012111 (2002).

[44] C.-P. Liu, M. J. Ramsey-Musolf, W. C. Haxton, R. G. E. Timmermans, and A. E. L. Dieperink, Phys. Rev. C **76**, 035503 (2007).

[45] R. A. Sen'kov, N. Auerbach, V. V. Flambaum, and V. G. Zelevinsky, Phys. Rev. A **77**, 014101 (2008).

[46] V. F. Dmitriev and R. A. Sen'kov, Phys. Rev. Lett. **91**, 212303 (2003).

[47] C. A. Baker *et al.*, Phys. Rev. Lett. **97**, 131801 (2006).

[48] V. V. Flambaum, I. B. Khriplovich, and O. P. Sushkov, Phys. Lett. B **162**, 213 (1985).

[49] V. F. Dmitriev and R. A. Sen'kov, Phys. At. Nucl. **66**, 1940 (2003).

[50] V. F. Dmitriev, R. A. Sen'kov, and N. Auerbach, Phys. Rev. C **71**, 035501 (2005).

[51] J. H. de Jesus and J. Engel, Phys. Rev. C **72**, 045503 (2005).

[52] S. Ban, J. Dobaczewski, J. Engel, and A. Shukla, Phys. Rev. C **82**, 015501 (2010).

[53] W. C. Haxton and E. M. Henley, Phys. Rev. Lett. **51**, 1937 (1983).

[54] R. J. Crewther, P. di Vecchia, G. Veneziano, and E. Witten, Appl. Phys. B **88**, 123 (1979).

[55] R. J. Crewther, P. di Vecchia, G. Veneziano, and E. Witten, Phys. Lett. B **91**, 487 (1980).

[56] M. Pospelov and A. Ritz, Phys. Rev. Lett. **83**, 2526 (1999).

[57] R. D. Peccei and H. R. Quinn, Phys. Rev. Lett. **38**, 1440 (1977).

[58] M. Pospelov, Phys. Lett. B **530**, 123 (2002).

[59] D. Cho, K. Sangster, and E. A. Hinds, Phys. Rev. A **44**, 2783 (1991).

[60] M. Pospelov and A. Ritz, Ann. Phys. **318**, 119 (2005).

[61] A. N. Petrov, N. S. Mosyagin, T. A. Isaev, A. V. Titov, V. F. Ezhov, E. Eliav, and U. Kaldor, Phys. Rev. Lett. **88**, 073001 (2002).

[62] B. K. Sahoo, B. P. Das, R. K. Chaudhuri, D. Mukherjee, and E. P. Venugopal, Phys. Rev. A **78**, 010501 (2008).

[63] T. Falk, K. A. Olive, M. Pospelov, and R. Roiban, Nucl. Phys. B **560**, 3 (1999).

[64] K. A. Olive, M. Pospelov, A. Ritz, and Y. Santoso, Phys. Rev. D **72**, 075001 (2005).